Profile Scale Spaces for Statistical Image Match in Bayesian Segmentation

Sean Ho

A dissertation submitted to the faculty of the University of North Carolina at Chapel Hill in partial fulfillment of the requirements for the degree of Doctor of Philosophy in the Department of Computer Science.

Chapel Hill
2004

Approved by

Advisor: Professor Guido Gerig, Ph.D.

Reader: Professor Stephen M. Pizer, Ph.D.

Reader: Professor Sarang Joshi, Ph.D.

Reader: Professor J. S. Marron, Ph.D.

Reader: Professor Elizabeth Bullitt, M.D.

ABSTRACT

SEAN HO: Profile Scale Spaces for Statistical Image Match
in Bayesian Segmentation
(Under the direction of Guido Gerig, Ph.D.)

Object boundaries in images often exhibit a complex greylevel appearance, and modeling of that greylevel appearance is important in Bayesian segmentation. Traditional image match models such as gradient magnitude or static templates are insufficient to model complex and variable appearance at the object boundary, in the presence of image noise, jitter in correspondence, and variability in a population of objects.

I present a new image match model for Bayesian segmentation that is statistical, multiscale, and uses a non-Euclidean object-intrinsic coordinate system. The segmentation framework is based on the spherical harmonics object representation and segmentation framework of Kelemen et al., which in turn uses the profile-based image match model of Active Shape Models. The traditional profile model does not take advantage of the expected high degree of correlation between adjacent profiles along the boundary. My new multiscale image match model uses a *profile scale space*, which blurs along the boundary but not across the boundary. This blurring is done not in Euclidean space but in an object-intrinsic coordinate system provided by the geometric representation of the object. Blurring is done on the sphere via a spherical harmonic decomposition; thus, spherical harmonics are used both in the geometric representation as well as the image profile representation. The profile scale space is sampled after the fashion of the Laplacian pyramid; the resulting tree of features is used to build a Markov Random Field probability distribution for Bayesian image match.

Results are shown on a large dataset of 114 segmented caudates in T1-weighted magnetic resonance images (MRI). The image match model is evaluated on the basis of generalizability, specificity, and variance; it is compared against the traditional single-scale profile model. The image match model is also evaluated in the context of a full segmentation framework, when optimized together with a shape prior. I test whether automatic segmentations using my multiscale profile model come closer to the manual expert segmentations than automatic segmentations using the single-scale profile model do. Results are compared against intra-rater and inter-rater reliability of manual segmentations.

ACKNOWLEDGEMENTS

The research presented in this dissertation was not a solo effort; there are numerous people who have contributed in one way or another to the development of this work.

My advisor, Guido Gerig, has been my close mentor throughout my entire time at UNC-Chapel Hill, and I am deeply indebted to him both for giving me freedom to pursue my own ideas and for nudging me to finish when I needed motivation. His constant patience and calmness have been an inspiration to me.

My thesis committee has been wonderfully open in giving me balanced feedback on my dissertation. Stephen Pizer spent considerable effort carefully reading my drafts under time pressure – pressure which was not due to his busy schedule but due to my procrastination. Sarang Joshi gave me honest and valuable feedback to keep my theory well-grounded and clearly elucidated. I have been privileged to have an esteemed statistician, Steve Marron, on my committee; I greatly appreciate his perspective, particularly his input on what statistical tests make sense for validation. Elizabeth Bullitt contributed her unique perspective as a neurosurgeon, providing insight on what is really needed in the clinic. I am indebted to her for being my unflagging cheerleader and advocate.

Two research labs outside of our MIDAG group deserve mention. The neuroimaging lab in the Psychiatry Department at UNC provided an excellent and large population of high-quality MR images with high-quality segmentations. These were created for longitudinal studies on autism and Fragile X syndrome, and I appreciate being allowed access to the data for training my statistical models. Thanks are extended to Joseph Piven, Rachel Gimpel, Michael Graves, Heather Cody Hazlett, and many others.

Another lab which deserves thanks is the Biomedical Imaging and Modeling group at the Technical University of Eindhoven in the Netherlands. The two weeks I spent

there in the summer of 2003 sparked many good ideas on the theory of scale space. I am indebted particularly to Remco Duits, as well as Bart ter Haar Romeny, Luc Florack, and many others at that lab.

Everyone within our MIDAG group at UNC deserves acknowledgement and thanks for being both colleagues and friends: Martin Styner, Conglin Lu, Yoni Fridman, Mark Foskey, Tom Fletcher, Joshua Stough, Eli Broadhurst, Christine Xu, and many others. I also acknowledge the support of a number of NIH grants throughout my time as a research assistant at UNC, including the MIP grant NIH-NIBIB P01 EB002779.

My family is a part of who I am; whatever credit goes to me should go to them in equal portion. I realize how blessed I am in having a warm and loving family; this is from the grace of God and nothing I deserve. My friends and church family at the Chinese Bible Church of North Carolina have been a solace and encouragement to me throughout these six years; I especially thank my close friends Dan Tan and Vinny Tang.

I am nothing without my Savior Jesus Christ. As I learn more about this field of medical image analysis, I see that in the marvelously intricate design of the human brain, in its inner workings that we understand so little of, in the incredible human visual system that performs automatically what our computer vision algorithms struggle to emulate, there is overwhelming evidence pointing to our Designer and Creator. Just as we computer scientists invest so much effort into our designs, so also our Creator invests in us and loves us. As I acknowledge all people in my life who have helped me, I acknowledge even more my Creator who loves me and sent His Son Jesus Christ to die for me and all mankind, bridging the gap between man and God. He alone deserves all glory.

> "If you confess with your mouth Jesus as Lord, and believe in your heart that God raised Him from the dead, you will be saved; for with the heart a person believes, resulting in righteousness, and with the mouth he confesses, resulting in salvation." (Romans 10:9-10, NASB)

CONTENTS

LIST OF FIGURES

CHAPTER 1

Introduction

1.1. Bayesian Segmentation

Segmentation is the task of delineating an object of interest from an image. The input to a segmentation process is an image to be segmented; the output is a description of the object of interest. This definition implies three key ingredients of segmentation:

(1) the object,
(2) interest, and
(3) the image.

What is meant by "the object"? In order to describe the object, a *geometric representation* is needed of the object. What is meant by an object "of interest"? The segmentation task does not look for random objects in the image, but it is supervised or *trained* to look for the particular object that the user is interested in. What is meant by "the image"? The *image representation* output by the image acquisition process (e.g., a digital camera, or reconstructed magnetic resonance image (MRI), or computed tomography (CT) image) is usually a scalar intensity field defined on 2D or 3D Euclidean space. These three ingredients motivate model-based segmentation schemes.

There are many geometric models in use today; a large class of geometric representations is the class of deformable shape models. A deformable shape model uses a template (or average) shape model that can be perturbed or instantiated to fit the target image. For example, a simple description of an object as a circle of radius r centered at position (x, y) is a geometric representation A deformable model for circles might adjust the

radius r and center (x, y) in order to fit to circles within the image, according to some definition of "fitting". This describes, as an example, the well-known Hough transform.

It is not often useful, however, to randomly search for all circles in an image; frequently, there is a particular object within the image that the user is interested in. This motivates a shift away from general-purpose segmentation algorithms and towards segmentation frameworks that can be trained to segment a specific object. A number of geometric models in current research are *statistical* shape models, trained on a number of "gold standard" expert segmentations drawn by hand. A shape representation is obtained of each of the objects in the training population, and a statistical model is built on the population of shape descriptors. This statistical model can then be used to guide the deformation of the shape model in segmentation. In the same way, there is motivation for the image to be represented via a statistical model, at least in a region of interest around the object.

In recent deformable-models segmentation work, image representation generally has not been dwelt upon as much as geometry representation: an image often is defined simply as a scalar function on a bounded (usually rectangular) region of Euclidean space ($\mathbb{R}^2$ for 2D images, $\mathbb{R}^3$ for 3D images). Multichannel images are sometimes used (e.g., RGB or multisequence MRI); then the image can be viewed as a tuple-valued function on Euclidean space. It is expected that data from the image will drive the deformation of the shape model. Local deformations are driven by local image features in a region of interest relative to the currently-deformed shape model. This motivates image representations (image sampling) in local, object-intrinsic coordinates.

For notation, let Ω represent the bounded subset of Euclidean space on which the image is defined (e.g., $\Omega \subset \mathbb{R}^3$ for a 3D image), and let $I : \Omega \to \mathbb{R}$ be the scalar image. Let m generically be the parameters of the shape model. Although some shape representations do not explicitly model the boundary of the object, the boundary manifold can generally be extracted from the shape representation, so call that boundary manifold $\mathcal{M}$. For simply connected 2D objects, $\mathcal{M}$ is a closed curve; for 3D objects, $\mathcal{M}$ is a 2D

manifold. Since $\mathcal{M}$ is assumed to be a manifold, it is differentiable. For this work, I assume that the object is simply connected; in 3D it is assumed that the boundary $\mathcal{M}$ is diffeomorphic to the sphere S^2.

Bayesian model-based segmentation phrases the segmentation task as an optimization problem – finding a shape that matches best to the training population of shapes while fitting best to the image. Bayes' rule is used to define the optimal shape m for a particular image:

$$
\begin{aligned}
(1) \qquad argmax_m p(m|I) &= argmax_m \frac{p(m,I)}{p(I)} \\
(2) \qquad &= argmax_m \frac{p(m)p(I|m)}{p(I)} \\
(3) \qquad &= argmax_m p(m)p(I|m)
\end{aligned}
$$

A Bayesian segmentation framework is described by defining the two probability distributions $p(m)$, the *prior* or geometric typicality, and $p(I|m)$, the *likelihood* or local image match. The geometric typicality $p(m)$ is guided by a model of the expected geometry and its variability within a population. Similarly, the image match $p(I|m)$ is guided by a model of the expected image appearance around the object. The deformable-models segmentation process starts by placing an initial object in the target image; this initialization is often the mean of the shape prior (defining the mean is not always trivial, though). At each iteration of the optimization, the image is sampled relative to the current deformation of the object. Image-based features are derived and compared with the image match model $p(I|m)$. The current deformation of the object is also compared with the shape prior $p(m)$. The object is then deformed in order to balance the shape prior with the likelihood, maximixing the product of the probabilities. If the object deforms into an unusual shape, then the shape typicality is decreased. If the image-based features around the object are not as expected, then the image match is decreased. The optimization is generally in a very high-dimensional feature space, with many local maxima.

1.2. Image Match

The focus in this dissertation is on the image match force $p(I|m)$, presuming that an appropriate geometric representation is chosen for the object and an appropriate shape prior $p(m)$ is defined. The image likelihood $p(I|m)$ is a probabilistic model of what the image I looks like relative to a given object geometry m. In Figure 1.1, the *corpus callosum* serves as an illustrative example. The corpus callosum (plural *corpora callosa*) is seen as a C-shaped light object in this midsagittal T1-weighted MRI slice. It has been segmented by the thick red contour. The image likelihood $p(I|m)$ seeks to model the image appearance in a collar of interest around the red contour. The image match model I propose is distinguished by three properties: it is statistical, multiscale, and uses object-intrinsic coordinates.

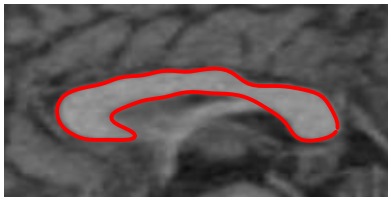

FIGURE 1.1. Midsagittal T1 MRI slice, showing corpus callosum outlined in red.

1.2.1. Statistical Image Match. Image match models can be classified broadly into *static* and *statistical* models. *Static* image match models have parameters that are fixed in advance. The classical image match force derived from gradient magnitude, described briefly in Section 2.1.1, is an example of a static image match model; the scale at which the gradient is taken is a global "knob" tweaked by the user. On the corpus callosum example, gradient magnitude works fairly well for most of the contour, since the image appearance across the boundary is well represented by a simple step edge of fixed scale. However, few anatomical objects are as simple in appearance as the corpus callosum.

Statistical image match models use parameters that are trained from a population of various segmented training images – images I_i each of which has a corresponding

segmentation m_i that is taken as the "ground-truth" of the geometry of the object. Figure 1.2 illustrates a small population of corpora callosa, from various patients, suitable for training a statistical model. The *model-building* process for a statistical image match model samples each of the training images I_i relative to the given geometry m_i to get an idea of what the image "looks like" near the object. This implicitly assumes a definition of *correspondence*, or homology, between objects in the training population. Generally the correspondence is given by the shape representation of the objects, sometimes augmented by manually-placed landmarks. Image-based features are derived from each of the training images, and the features are used to train the statistical image match model. A standard example of a statistical image match model is the one used by Active Shape Models; it is described in more detail in Section 2.1.3.1. The image match model proposed in this dissertation can be seen as an extension of the statistical image match model used by Active Shape Models.

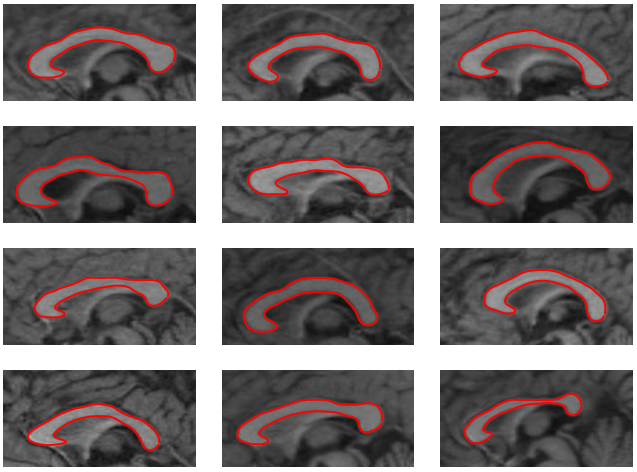

FIGURE 1.2. Population of corpora callosa, on which a statistical image match model could be trained.

1.2.2. Multiscale Image Match. Observations are taken with an aperture, and a signal may have components at various scales. The pixel size of an image, for instance an MRI, represents observations taken at a particular scale that is set by the image acquisition process. However, the object of interest within the image might be best represented

at other scales. Others have worked on multiscale object geometry representations [Pizer et al. 2003]; similarly, a multiscale representation of the image uses multiple apertures, from coarse to fine, to sample the image. A multiscale image model can show at various locations what are the scales at which the variability in the training population is represented most tightly. For instance, in the corpus callosum example, the bulk of the corpus callosum might be well-represented at a relatively large scale, since it is fairly uniform white matter with a fairly consistent step-edge at the boundary. However, the fornix (small white matter branch off the lower edge of the corpus callosum) is a relatively small scale feature, so the image intensities at that location might be well-represented at a relatively small scale. Classical single-scale image match models represent the image only at the original pixel scale provided by the image acquisition process, rather than finding natural local scales at which to represent the image, which may depend on the object geometry, correspondence, signal-to-noise ratio, and population variability. A number of image segmentation techniques have *multi-grid* extensions, which use multiscale techniques [Cootes et al. 1994, Willsky 2002]. The human visual system at some level uses a multiscale approach [Romeny 2003].

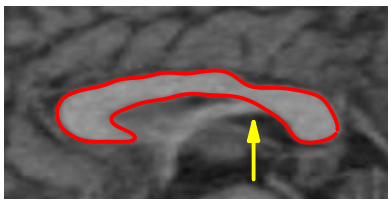

FIGURE 1.3. Segmented corpus callosum. Arrow indicates the fornix, a small scale white matter structure branching off from the lower boundary of the corpus callosum. Consistent localization of the fornix across the population motivates image match in object-intrinsic coordinates.

1.2.3. Image Match in Object-Intrinsic Coordinates. Object-intrinsic coordinates are a local non-Euclidean coordinate system on the object, derived from the geometry of the object, instead of the image acquisition process. The standard coordinate system for images, for instance the Euclidean (x, y, z) coordinate system of 3D MRI, is provided by the scanner in which the image was taken. If the orientation of a patient's head

changes relative to the scanner, then the orientation of objects in the standard image coordinate system changes as well. In the corpus callosum example, if it is desired to localize the fornix consistently across the population of corpora callosa, then a system of correspondence is needed that matches the fornix of one corpus callosum to the fornix of another. An object-intrinsic coordinate system is a way of representing a continuum of such correspondences in a region of interest around the object. The task of defining correspondence, or homology, is a large issue [Davies 2002, Styner et al. 2003] that is outside the scope of this work, but my image match method depends on having a correspondence given. If a different system of correspondence is provided, then my method can take advantage of it just as easily.

My implementation uses the spherical harmonics (SPHARM) shape representation for the object boundary, which decomposes the (x, y, z) coordinates of boundary points using spherical harmonic basis function. A system of correspondence based on an equal-area parameterization is also provided by this shape representation. The SPHARM shape representation will be described in Section 2.2 and in further detail by [Kelemen et al. 1999]. Potential extensions to other shape representations will be described in Section 5.4.5.

To sample the image using object-intrinsic coordinates instead of Euclidean image coordinates, I use image *profiles*. Profiles are samples taken from the image along 1-dimensional paths intersecting the object boundary. A collection of profiles about a particular geometric object within a particular image is a representation of the region within that image that is of interest for localizing the boundary. For example, profiles may capture a step-edge in intensity at the boundary of the corpus callosum. The particular profile sampling scheme I use will be discussed in more detail in Section 3.1.6.

1.3. Case Study: Caudate

Many segmentation methods use an image match that locally drives the object boundary to points of high image gradient magnitude. The classical "snakes" [Kass et al. 1987a],

for instance, uses this approach. In many objects, however, a simple gradient-magnitude based image match model is insufficient. The profile of the image across the object boundary can vary significantly from one portion of the boundary to another. Some portions of the boundary might not even have a visible contrast, in which case the shape prior may be needed to define the contour. In real-world medical images, the contrast-to-noise ratio is often low, and models need to be robust to image noise.

In this work, the target anatomical object for segmentation is the caudate nucleus in the human brain. From a partnership with the UNC Psychiatry Department, access is provided to over 100 high-resolution MRIs with high-quality manual expert segmentations of both left and right caudates. The manual raters, having spent much effort on developing a reliable protocol for manual segmentation, indicate some of the challenges in caudate segmentation, which motivate a multiscale statistical image match model for automatic methods.

A fraction of the surface of the caudate borders the lateral ventricle, providing strong contrast between the uniform grey matter of the caudate with the cerebro-spinal fluid (CSF) of the ventricle. Other portions of the caudate border white matter tracts, presenting a different image profile, which is still fairly consistent at corresponding locations across the training population.

Portions of the boundary of the caudate can be localized with standard edge detection (provided the appropriate scales are chosen). However, there are also nearby false edges that may be misleading. In addition, where the caudate borders the nucleus accumbens, there is no contrast at the boundary; the manual raters use a combination of shape prior and external landmarks to define this part of the boundary. Figure 1.4 shows the challenge. The caudate and nucleus accumbens are distinguishable on histological slides, but not on MRI of this resolution.

Another "trouble-spot" for the caudate is where it borders the putamen; there are "fingers" of cell bridges that span the gap between the two. The scale of the object structure relative to the scale of the image noise may swamp single-scale image match models

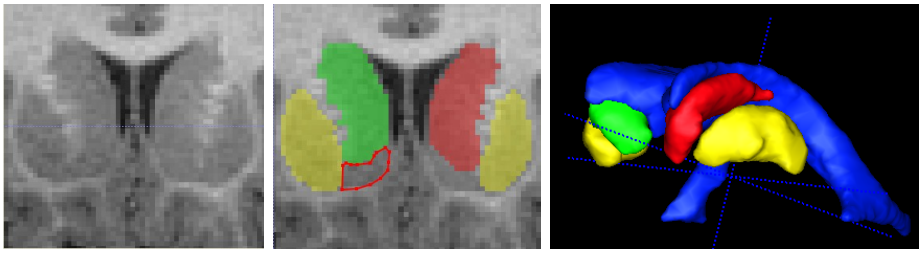

FIGURE 1.4. Coronal slice of the caudate: original T1-weighted MRI (left) and segmented (middle). Right and left caudate are shown shaded in green and red; left and right putamen are sketched in yellow, laterally exterior to the caudates. Nucleus accumbens is sketched in red outline. Note the lack of contrast at the boundary between the caudate and the nucleus accumbens, and the fine-scale cell bridges between the caudate and the putamen. At right is a 3D view of the segmented caudate and putamen relative to the ventricles. Figure courtesy of Rachel Gimpel.

with the noise. The fact that there are clinical names for these particular "trouble-spots" implies a need for *correspondence,* a mapping of homologous points between different instances of the same object. For example, the location of the nucleus accumbens relative to each patient's caudate is needed in order for the image match model to know that that location expects a different image appearance than elsewhere. The approach of this dissertation utilizes the object-intrinsic coordinate system given by the *SPHARM* geometric representation to formalize the correspondence. The surface of each object in the training population is mapped to a common coordinate system, in this case the unit sphere S^2.

Many other segmentation tasks in medical images present challenges similar to the caudate; in automatic segmentation methods, this motivates image match models that are statistically trained and multiscale.

1.4. Thesis

In this dissertation I propose a novel multiscale statistical model of image appearance in a collar of interest around an object boundary, suitable for use as image match likelihood in a Bayesian segmentation framework.

This model significantly improves specificity and variance over a classical single-scale profile model, as demonstrated on a large-scale MRI study of the caudate nucleus, evaluating generalizability, specificity, and variance. Validation also compares automatic segmentation using my image match model, automatic segmentation using a classical single-scale model, and expert manual segmentation.

1.5. Accomplishments

Much of the work in this dissertation builds upon existing work of others in the field. The novel contributions that I present include

- A scale space for functions on manifolds that are diffeomorphic to the sphere S^2,
- A scale space for boundary profiles of simply-connected objects, which is a new scale space in object-intrinsic coordinates,
- A probabilistic model for boundary profiles, using the above scale space,
- A complete, self-contained software framework for model-building and segmentation, using the above probabilistic model for image match,
- Validation of the results from the above segmentation framework, on a sizeable population of 114 caudate datasets, with manual rater segmentations,
- Evaluation of the generalizability, specificity, and statistical efficiency of the above probabilistic model for boundary profiles.

1.6. Overview of the Chapters

This dissertation is organized in five chapters. This chapter introduced the task at hand, namely the construction of a multiscale statistical image match model, and provided some motivation why such an image match model is useful. Chapter 2 will provide background material to the dissertation, discussing other image match models in use in popular Bayesian model-based segmentation schemes. Particular attention will be given to the *SPHARM* segmentation framework, upon which the shape prior of my work is based. The background chapter also will discuss various axiomatic approaches to scale

space. Chapter 3 will describe my multiscale statistical image match model. The first section in the chapter will define a scale space on image profiles taken about the boundary of the object in the image. The second section will describe features sampled from that profile scale space, which are then used in a Markov random field probabilistic model. Chapter 4 will describe the testbed implementation in *Mathematica*, the datasets used, and validation of the claims of the thesis. The image match model will be evaluated on its own as a probabilistic model; it will also be evaluated as a component of a complete segmentation framework in conjunction with a shape prior. Comparisons will be made of the new multiscale image match model against the classical single-scale image match model. Chapter 5 will conclude with proposed future work, possible extensions and new applications.

CHAPTER 2

Background

2.1. Image Match Models in Deformable-Models Segmentation

Deformable models have had a long history in image segmentation, and each method uses some form of image match to drive the deformable model into the target image. Image match is sometimes also referred to as "image energy" or "external forces", in contrast to the shape prior, or "internal forces". Even with non-Bayesian segmentation models, there is always a driving force that instantiates the model into a particular target image. The focus of this dissertation is a new multiscale statistical image match model; in this chapter I present a selection of existing image match models in use in deformable-models image segmentation.

2.1.1. Gradient Magnitude "Edge Finding". Perhaps the simplest image match model is simply to use the magnitude of the gradient vector of the image intensity field. In the classical snakes [Kass et al. 1987b], the image match force pushes each contour point towards a local maximum of image gradient magnitude. The degree of match of the whole contour into the image is the integral along the contour C of the local image gradient magnitude $|\nabla I|$:

$$p(I|m) \propto \int_C |\nabla I(x)| dx.$$

This integral does not yield a probability distribution on its own, but the Bayesian image match probability distribution is usually some monotonic function of the integral of gradient magnitude.

The gradient magnitude is one example of a translation and rotation invariant feature that can be used to drive the image force. Other examples include the Harris corner detector [Harris and Stephens 1988] and affine-invariant corner detectors [Blom 1991].

Gradient magnitude is often used by both mesh-based snakes and implicit (geodesic) snakes [Malladi et al. 1995, Caselles et al. 1997]. This works well for clearly defined objects whose boundary is always characterized by a sharp discontinuity in image intensity. However, this image match model is global (it assumes the boundary appearance is uniform across the whole object) and static (it is not statistically trained). The gradient magnitude is often calculated at a fixed scale at all points along the contour; hence it assumes that the desired edges in the image are all at the same scale. Gradient magnitude image match performs poorly at weak or nonexistent step edges, or when the boundary discontinuity is not well-represented by a step edge.

2.1.2. Static Template Matching.

2.1.2.1. *Inside/Outside Classification.* Region-competition snakes use global probability distributions of "inside" intensities vs. "outside" intensities to drive the image match [Zhu and Yuille 1995, Tek and Kimia 1997]. van Ginneken et al. perform a local inside/outside classification using not just the raw greylevels but a high-dimensional n-jet feature vector, with k nearest-neighbor (k-NN) clustering and feature selection, based on the training population [van Ginneken et al. 2001]. Leventon et al. train a global profile model that relates intensity values to signed distances from the boundary, incorporating more information than a simple inside/outside classifier [Leventon et al. 2000].

2.1.2.2. *Profile Templates.* Segmentation via registration to a template image or atlas is a common technique.

For example, the medially-based m-reps deformable model segmentation framework [Joshi et al. 2001] can use image intensities taken from a single template image to drive its image match forces. The normalized correlation between corresponding intensities in the template image and in the target image provides the image match. This takes advantage of the correspondence given by the medially-defined figural coordinate system in a

volumetric collar about the object boundary, implied from the geometric representation. Normalized correlation is equivalent to a local Gaussian model on each profile, where the mean is the template profile and the covariance matrix is diagonal. It assumes that intensities at different positions along the profile are uncorrelated. The profile model which I will present explicitly models the correlation between intensities at different positions along a profile, as well as the correlation between adjacent profiles along the boundary.

Profiles have also been used in 2D cardiac MR images [Duta et al. 1999]. Fenster et al. have extracted features from profiles for use in fitting their Sectored Snakes [Fenster and Kender 2001].

2.1.2.3. *Image Warping.* In the fluid warping techniques of Joshi et al. [Miller et al. 1999], a template image is warped to the target image via a diffeomorphic map. Manually-placed landmarks in both template and target images guide the optimization of the diffeomorphic map, but the match between template and target images is measured by the integrated squared-difference between image intensities in MRI:

$$D(h) = \int_{\Omega} |T(h(x)) - S(x)|^2 dx, \tag{4}$$

where $T(h(x))$ is a sample from the warped template image, $S(x)$ is a sample from the target image, and Ω is the region of interest. The image energy term in the optimization is a combination of $D(h)$ and a term that optimizes the manually-placed landmarks.

Image match by profile templates can be seen as a special case of image match by fluid warping, where the region of interest is the collar about the boundary where the profiles are taken. Joshi et al. also take special care to ensure the warp from target image to template image is diffeomorphic.

2.1.2.4. *Mutual Information.* The sum of squared-differences in image intensity is not the only metric of image match that can be used to match the template to the target image. For example, recent work of Tsai et al. uses mutual-information between regions of the image and a label map to drive the segmentation [Tsai et al. 2003, 2004]. Willis [2001] also use mutual information between a template image and the warped target image.

2.1.3. Probabilistic Models.

2.1.3.1. *Statistical Profile Model.* Cootes and Taylor's seminal Active Shape Model work [Cootes et al. 1993] samples images along 1D profiles around boundary points, normal to the boundary, using correspondence given by the Point Distribution Model of geometry. At each point along the boundary, a probability distribution is trained on the image-derived features in the 1D profile (ASMs use the derivative of image intensity along the profile). The corresponding profile is sampled from the target image, and the Mahalanobis distance in the probability distribution at that boundary point provides the image match. Recently Scott et al. expanded the feature space used in the profiles [Scott et al. 2003].

The ASM profile model has been used with 2D Fourier [Staib and Duncan 1992] coefficients as the shape representation instead of PDMs.

A statistical model built from a few select profiles was also described by Duta et al. and applied to cardiac MR images [Duta et al. 1999].

The "hedgehog" model in the spherical harmonic segmentation framework [Kelemen et al. 1999] uses a training population linked with correspondence from the geometric model. It can be extended with a coarse-to-fine sampling of the object boundary in order to improve robustness in the face of image noise and jitter in correspondence.

Recent work by Stough et al. on profiles for m-reps uses clustering to elect a small number of representative profile types, then classifies boundary patches according to profile type [Stough et al. 2004].

Van Ginneken [van Ginneken et al. 2001] discriminates between profiles at correct boundary positions and profiles shifted normal to the boundary, for use in localizing the object boundary.

2.1.3.2. *Active Appearance Models.* A different approach is taken by Cootes and Taylor's Active Appearance Models [Cootes et al. 2001], which use the point correspondences given by an ASM to warp images into a common coordinate system, within a region of interest across the whole object, given by a triangulation of the PDM. A global Principal Components Analysis is performed on the intensities across the whole object (the size

of the feature space is the number of pixels in the region of interest). To improve the optimization process, global PCA are performed on the registered images blurred at various scales. The use of a global PCA is particularly well-suited for capturing global illumination changes, for instance in Cootes and Taylor's face recognition applications.

2.1.4. Summary and Limitations of Existing Work. Real world images and also medical imagery, for example, exhibit complex discontinuities at the object boundary. Moreover, discontinuities can have different characteristics at different locations along the boundary. For instance, object could be expected to have a step edge at one part of the boundary but a line-like edge at another part along the boundary. It is clear that gradient magnitude, especially at fixed global scale, is not sufficient to capture complex image characteristics. A robust image match model also needs to be trained from a population of images; a single template is not sufficient. Current profile models capture local variation, but they do not take advantage of the expected high degree of correlation between adjacent profiles along the boundary. Normalization of the profiles is also an issue; selection of appropriate image-derived features is important. Active Appearance Models are very promising and closely related; this work can be interpreted as an extension of ASMs to capture local intensity variation in a hierarchical fashion.

It is desired that an image match model be robust enough to capture local intensity-derived features about the boundary, while being aware of the distinction between the *along-boundary* and *across-boundary* directions, already defined by the geometric model. Across the boundary, one would like to know if the image locally should be expected to present a step edge, or a line-like edge, or something else, at different scales. Along the boundary, one would like to take advantage of spatial locality in order to provide robustness to image noise and jitter in the provided correspondence. The image characteristics about a single point on the boundary may be noisy and difficult to model, but perhaps by averaging over a larger portion of the boundary, it may be evident that a line-like edge for instance is expected at this patch of the object boundary.

It is also important that a framework exists for examining the training images sampled at corresponding points so that statistical models can be built of the intensity variation about the boundary. There are many potential sources of image noise in the image acquisition process. For instance, in MRIs, challenges include MR noise, scanner stability, and bias field inhomogeneity, in addition to patient induced variations of brightness and contrast as well as inter-object variability (e.g., motion of adjacent structures). An image match model is desired that can capture image characteristics about the object boundary despite noise, in order to improve segmentation.

Image features at the boundary may appear at various scales, which motivates a multiscale approach. However, traditional multiscale features blur in Euclidean space, which may blur across the object boundary. In the spirit of Canny [Canny 1986], multiscale features are desired where the blurring is along the boundary and not across the boundary.

My approach is to construct a *scale space* on the image profiles, similar to classical scale-spaces [Koenderink 1984, Florack et al. 1996] but on a curved non-Euclidean space. I then sample the profile scale space after the fashion of Laplacian image pyramids [Burt and Adelson 1983] to obtain multiscale features upon which Gaussian models are trained using the training population. The end result is a likelihood model for geometry-to-image match; this combined with the shape prior produces the posterior that is to be optimized in Bayesian segmentation.

2.2. The *SPHARM* Segmentation Framework

Any image match model for Bayesian segmentation will be closely tied to the geometric representation used for the object to be segmented – whether a boundary representation, medial representation, volumetric representation, or other representation of the object. The general concept presented in this dissertation is applicable to various geometric representations, but the details are necessarily tied to a particular geometric representation. I choose to use the *SPHARM* shape representation of Brechbühler et al. [C. Brechbühler and Kubler 1995]. Kelemen et al [Kelemen et al. 1999] used this shape representation in conjunction with an ASM-style single-scale statistical profile model to produce a full Bayesian segmentation framework. This section is a brief review of that work; for more details refer to the above citations and the dissertations of Brechühler and Kelemen.

The *SPHARM* shape representation uses an orthogonal basis expansion of the (x, y, z) coordinates of points on the object boundary. The spherical harmonics $\{Y_l^m\}$ are a complete orthonormal basis for $L^2(S^2)$, functions on the unit sphere S^2. The exact definition will be given in Section 3.1.2. A mesh of equally-spaced points $\{(x_i, y_i, z_i)\}$ on the surface of the simply-connected object is parameterized by three functions $(x(\theta, \phi), y(\theta, \phi), z(\theta, \phi))$ on S^2; each is expanded in the spherical harmonic basis:

$$x(\theta, \phi) = \sum_{l,m} {c_{xl}}^m Y_l^m(\theta, \phi) \tag{5}$$

$$y(\theta, \phi) = \sum_{l,m} {c_{yl}}^m Y_l^m(\theta, \phi) \tag{6}$$

$$z(\theta, \phi) = \sum_{l,m} {c_{zl}}^m Y_l^m(\theta, \phi). \tag{7}$$

The set of spherical harmonic coefficents $\{\mathbf{c}_l^m\} = \{({c_{xl}}^m, {c_{yl}}^m, {c_{zl}}^m)\}$ forms the geometric representation of the object. The abbreviation *SPHARM* is used to refer to these $\{\mathbf{c}_l^m\}$ as a shape representation, or to refer to Kelemen's complete segmentation framework using this shape representation ("the *SPHARM* segmentation framework").

The parameterization of the surface of the object, in the form of the three functions $(x(\theta,\phi), y(\theta,\phi), z(\theta,\phi)$, is itself a complex optimization problem. The parameterization is constrained to preserve areas: patches of equal area on the original object map to patches of equal area on the parameter space (S^2). Angles cannot be preserved exactly, but squares on the original object are optimized to map to approximate squares on S^2. This parameterization defines a point-to-point correspondence between instances of an object: for example, it defines a north pole on each of the instances of an object. My implementation uses the equal-area parameterization given by *SPHARM*s, but the method can take advantage of other definitions of correspondence when provided.

A reasonable shape prior for a Bayesian segmentation framework using the *SPHARM* shape representation is a Gaussian distribution on the spherical harmonic coefficients $\{\mathbf{c}_l^m\}$ of normalized objects. The surface of each object in the training population is parameterized and expanded in the spherical harmonic basis. The coefficients are then normalized to factor out global translation and rotation, and a multidimensional Gaussian model is built on the resulting normalized coefficients:

$$p(m) = p(\{\mathbf{c}_l^m\}) \tag{8}$$

$$= N(\mu_c, \Sigma_c)(\mathbf{c}), \tag{9}$$

where $N(\mu_c, \Sigma_c)(\mathbf{c})$ represents the Gaussian likelihood of the coefficient set $\mathbf{c}$ in the multidimensional normal distribution with mean shape μ_c and covariance matrix Σ_c. In usual implementation, the spherical harmonics are expanded to order 12, resulting in a feature space of dimension 504. This is the shape prior used in this dissertation work.

Kelemen's *SPHARM* segmentation framework is inspired by ASMs and does not in fact use the above Gaussian shape prior model; rather, it uses a constrained optimization approach where the segmentation is allowed to deform freely within a box of "allowable" shapes (e.g., within ± 2 standard deviations in the first five eigenmodes of deformation). This is equivalent to a shape prior that is uniform within the box of allowable shapes and zero outside the box.

The image match model in Kelemen's *SPHARM* segmentation framework uses image profiles at the object boundary. The *SPHARM* shape representation provides a parameterized surface for the boundary of the object, which in particular allows normals to the boundary to be computed analytically. For each object in the training population, its corresponding image is sampled along a number of straight lines perpendicular to the boundary and crossing it. Section 3.1.6 will discuss the issue of how profiles are sampled: I use the same sampling method as the *SPHARM* framework does, but it does have a number of problems. Figure 2.1 illustrates the locations from which profile samples are taken; they appear like quills on a hedgehog. Thus for each object n in the training population, at each corresponding location i on the boundary, there is a vector $\mathbf{u}_i^n$ of image intensities sampled across the boundary. In sample implementations there may be 114 training objects, 512 profiles around the object boundary, and 11 samples along each profile.

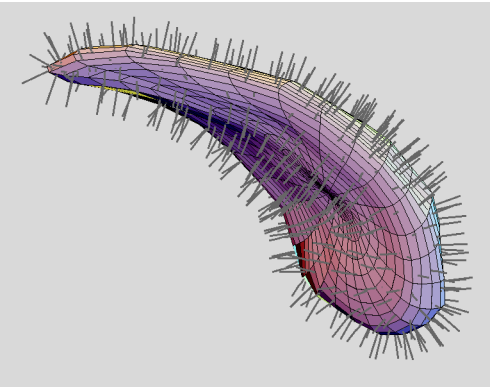

FIGURE 2.1. Visualization of the profiles extracted from the boundary of the caudate. Profiles are shown as white "quills" normal to the boundary.

In the single-scale profile model used by Kelemen and inspired by ASMs, each position along the boundary has an independent Gaussian profile model: each $\mathbf{u}_i$ is modeled by its own normal distribution $N(\mu_i, \Sigma_i)$. With the above numbers, there would be 512 independent 11-dimensional Gaussians. The overall Bayesian likelihood is simply the

average of the likelihoods at each profile:

$$p(I|m) = p(\{\mathbf{u}_i\}) \tag{10}$$

$$= \frac{1}{N}\sum_i p(\mathbf{u}_i) \tag{11}$$

$$= \frac{1}{N}\sum_i N(\mu_i, \Sigma_i)(\mathbf{u}_i), \tag{12}$$

where N is the number of profiles around the boundary (e.g., 512). $N(\mu_i, \Sigma_i)(\mathbf{u}_i)$ represents the Gaussian likelihood of $\mathbf{u}_i$ in the multidimensional normal distribution with mean μ_i and covariance matrix Σ_i.

During segmentation, at each iteration of deformation the spherical harmonic coefficients $\mathbf{c}$ are calculated from the deformed shape and compared against the shape prior model. Profiles $\mathbf{u}$ are also taken from the deformed segmentation and compared against the image match models. Each profile $\mathbf{u}_i$ is fit against the local profile model at various shifts normal to the boundary; the optimal shift is a suggested local deformation of the boundary. The suggested deformations $\mathbf{dx}$ are transformed into perturbations $\mathbf{db}$ in the shape eigenspace and constrained to lie within the "box" of allowable deformations.

In this dissertation I use the *SPHARM* shape representation and segmentation framework as a platform to explore multiscale extensions to the profile model with a non-Euclidean scale space that follows the object boundary. The testbed implementation uses a Gaussian shape prior as described above. It allows comparison of the conventional single-scale profile model to my new multiscale profile model. The implementation will be described in more detail in Section 4.1.

2.3. Approaches to Scale Space

Since my new image match model is a multiscale extension to the standard profile model used in ASMs and Kelemen's *SPHARM*s, I review a selection of prior work on the issue of scale from the perspective of scale space. Observations are always taken at scale; the original resolution of the image is only a result of the image acquisition process. The natural scale at which objects or signals exist may be different from the image acquisition resolution. In addition, fine-scale image noise often clouds the signal, and this motivates multiscale approaches that can model the signal at its appropriate scale while separating out the image noise.

A *scale space* is an image defined on the product space of the domain of the original image with the *scale axis* $\mathbb{R}^+$; it is a way of representing an image at all scales simultaneously. If the original image is a scalar function in d-dimensions, $f : \mathbb{R}^d \to \mathbb{R}$, a scale space of f would be a function $\Phi(f) : \mathbb{R}^d \times \mathbb{R}^+ \to \mathbb{R}$. I define an observation at scale as a particular point in scale space; how scale space is constructed defines what is meant by "scale". For a given scale σ, a cross-section $\{\Phi(f)(\mathbf{x}, \sigma) : \mathbf{x} \in \mathbb{R}^d\}$ through the scale space represents the image blurred at scale σ. Figure 2.2 shows an illustration of a *scale-stack* in $\mathbb{R}^2 \times \mathbb{R}^+$, a number of slices through the scale space at various scales σ.

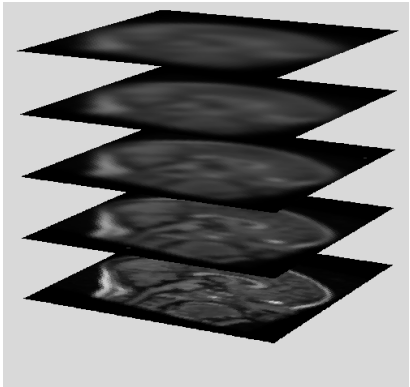

FIGURE 2.2. Illustration of a scale-stack, a sampling of continuous scale space that is discrete in scale. Shown are scales $\sigma = 0.5$, 1.5, 2.5, 3.5, and 4.5.

The scale-stack is discrete in scale, but scale space is continuous in scale, and hence allows cross-sections in different directions. For example, Figure 2.3 shows an illustration of a cross-section through scale space that is continuous in both x and σ directions.

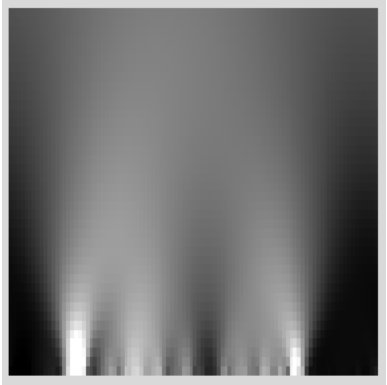

FIGURE 2.3. Illustration of a vertical cross-section through scale space, showing the continuous representation in scale (vertical axis).

In Euclidean space $\mathbb{R}^d$, a classical definition of linear scale space is that which is obtained by Gausssian blurring of the original image at scale σ:

$$\Phi(f)(x, y; \sigma) = (G_\sigma \circ f)(x, y) \tag{13}$$

$$= \frac{1}{\left(\sqrt{2\pi}\sigma\right)^d} \int f(\mathbf{x} + \mathbf{\Delta x}) e^{-\frac{|\mathbf{\Delta x}|^2}{2\sigma^2}} \, \mathrm{d}\mathbf{\Delta x}, \tag{14}$$

where G_σ denotes the zero-mean Gaussian kernel of standard deviation σ and $\circ$ denotes convolution.

Scale space has been approached in many different ways; most definitions of linear scale space in Euclidean space include the Gaussian scale space as one case. Many approaches to scale space are axiomatic, starting from a list of desired properties of scale space and deriving a unique definition that satisfies those properties.

For example, the earliest known axiomatic derivation of scale space is by Iijima; his little-known journal article in Japan was recently reviewed in [Weickert et al. 1999]. It consists of five axioms: linearity, shift invariance, scale invariance, the semigroup property, and positivity. Linearity with respect to multiplication specifies that the scale space of a function whose values have all been scaled by a constant factor λ should be

obtainable by multiplying the values of the original scale space by the same factor:

$$\Phi(\lambda f) = \lambda \Phi(f). \tag{15}$$

Shift invariance specifies that the scale space of a translated function should just be the translated scale space of the original function:

$$\Phi(T_{s_0}(f)) = T_{s_0}(\Phi(f)), \tag{16}$$

where T_{s_0} represents a translation operator acting on functions, shifting by an amount s_0. In $\mathbb{R}^d$, $T_{\mathbf{x}_0}(f)(\mathbf{x}) = f(\mathbf{x} - \mathbf{x}_0)$. Scale invariance requires that the scale-space operator should be invariant to the scale of a function:

$$\Phi(S_c(f)) = S_c(\Phi(f)), \tag{17}$$

where S_c represents a scaling operator acting on functions, enlarging the scale of the function by a factor c. In $\mathbb{R}^d$, $S_c(f)(\mathbf{x}) = f(\mathbf{x}/c)$. The semigroup property means that blurring via the scale space should "cascade":

$$\Phi(f_{\sigma_1})(s, \sigma_2) = \Phi(f)(s, \sigma_1 + \sigma_2), \tag{18}$$

where $f_{\sigma_1}(s) = \Phi(f)(s, \sigma_1)$ as above. The axiom of positivity specifies that the scale space of an everywhere-positive function should be everywhere-positive:

$$f(s) > 0 \quad \forall s \implies \Phi(f)(s, \sigma) > 0 \quad \forall s, \sigma. \tag{19}$$

As a boundary condition ensuring that the scale space represents the original signal at zero scale, one more axiom is added requiring that the scale space of a function f converge uniformly to f as the scale σ goes to 0.

Iijima's axiomatic is only one set of axioms for scale space, though, and there are others. Florack uses another set of axioms, starting from linearity, shift invariance, and scale invariance, and adding isotropy (rotation invariance) [Florack et al. 1992].

ter Haar Romeny has used similar axiomatics derived from the human front-end vision system [Romeny 2003].

Koenderink introduced the axiom of *causality*, that no new information should be created as one goes up in scale (to coarser scale). His early foundational work used this axiom together with linearity and isotropy to derive the Gaussian scale space [Koenderink 1984]. A concise overview diagram of a number of scale space axiomatics is in [Kuijper 2003].

An observation made by Koenderink, ter Haar Romeny, Lindeberg [Lindeberg 1994], and others is that a number of standard axioms for scale space lead to a particular partial differential equation which the scale space needs to satisfy, namely, the *heat equation*:

$$\frac{\partial u}{\partial t} = \triangle u. \tag{20}$$

Boundary conditions on the solution specify that as the scale parameter t goes to zero, u approaches the original image f. The linear operator $\triangle$ can also be expressed as $div(\nabla u)$. The heat equation approach to scale space will be discussed in more detail in Section 3.1.1. This is the approach to scale space that I adopt: in Chapter 3 a scale space will be proposed as a solution to the heat equation in a non-Euclidean space.

Duits has modified the heat equation by adding a fractional power $\alpha \in (0, 1]$ to the linear operator $\triangle$:

$$\frac{\partial u}{\partial t} = -(-\triangle)^{\alpha} u. \tag{21}$$

This results in a family of scale-spaces, of which the Gaussian scale space is a special case at $\alpha = 1$. The case $\alpha = 1/2$ leads to a scale space generated by the Poisson operator. The α scale spaces satisfy all the classical axioms of scale space, using a weak version of the causality axiom [Duits et al. 2004].

Various non-linear scale-spaces have also been described on the Euclidean domain; they violate the axiom of linearity but can be useful for edge-enhancement. For example, Perona and Malik proposed a non-linear diffusion process that modifies the classical heat

equation to become

$$u(\mathbf{x}, t) = div \cdot (g(|\nabla f|)\nabla f)\,, \tag{22}$$

where g is a monotonically decreasing function [Perona and Malik 1990]. The idea is to reduce the blurring around "edges" (as detected by $g(|\nabla f|)$) so as to preserve the edge structure. Anisotropic diffusion blurs in different amounts along different directions; the aim is to blur parallel to an edge but not across the edge [ter Haar Romeny 1994].

These non-linear and anisotropic scale spaces use local image information (such as the image gradient) to determine where to blur and in what directions to blur. The scale space I will define is inspired by the same concept of blurring along the boundary but not across it. However, rather than the image gradient, my method uses the boundary given by the segmentation geometry. The blurring is performed using not the Euclidean metric, but a metric implied by the geometric representation of the object: an object-intrinsic coordinate system. The *profile scale space* I will define in the next chapter takes advantage of a definition of correspondence given by the geometric representation.

CHAPTER 3

Methods

My objective in this dissertation is to define a measure of geometry-to-image match, i.e., a measure of how well a given geometric object fits into a target image. Such a measure is specified as a probability distribution on image intensity features in a region of interest about the object boundary. In this chapter, the image features are defined and a probability distribution is then imposed on those features. An important construct defined here is the *profile scale space*, which allows analysis of image profiles of the boundary at various scales, while not blurring away contrast across the boundary. The profile scale space is sampled according to a hierarchical tree structure, and the resulting multiscale image features, across the training population, are modeled with a Markov Random Field probability distribution. Throughout this chapter, the notation is specific to objects in 3D images, but most of the theory can be extended naturally to arbitrary dimension.

I start in Section 3.1.1 by discussing my approach to scale space from the perspective of the heat equation and the Laplacian operator. This approach allows me to define in Section 3.1.2 a scale space for scalar-valued functions defined on the sphere S^2. The sphere is simpler geometrically than the boundary of a generic object, but it still presents some interesting challenges in comparison to Euclidean space.

Section 3.1.3 makes use of the scale space on S^2 to define a scale space for scalar functions on arbitrary object boundaries that are diffeomorphic to S^2, via a diffeomorphic mapping provided by a spherical harmonic representation of the object. This scale space is not the same as that obtained by Laplace-Beltrami smoothing; Section 3.1.4 briefly compares the two.

In Section 3.1.5, I review a few properties that have been used as axioms to classical derivations of scale space on Euclidean space. I then discuss those scale-space properties that apply to these non-Euclidean domains, and I discuss whether my definition of scale space satisfies these properties.

Section 3.1.6 then extends the scale-space concept from scalar-valued functions to profiles across the object boundary, viewed as a product space of the boundary manifold with the interval $[-1, 1]$.

With the profile scale space defined, Section 3.2.1 describes a multiscale collection of features sampled from the profile scale space. In the model-building phase these features are extracted from each of the segmented training images and used to train a Markov Random Field probabilistic model, as is described in Section 3.2.2. During segmentation the same image features are extracted from the target image relative to the deformable shape model in its current state of deformation. The probabilistic model defines the match of the deformed shape model to the image.

3.1. The Profile Scale Space

3.1.1. Scale Space and the Heat Equation. To use multiscale features in modeling the image, I first must define what is meant by scale. For instance, the boundary of a particular object might be well-represented by a step-edge at a large patch of the boundary; however, when the image is sampled at too fine of a scale, the image noise overwhelms the edge structure. The aim is that a multiscale representation of such a boundary patch could capture efficiently the step-edge profile at a large scale along the boundary, while separating out the fine-scale noise.

As discussed in Section 2.3, classical scale-space theory in Euclidean space has often used the analogy of heat distribution on a conducting plate [Lindeberg 1994]. The original signal represents an initial distribution of heat on the plate; certain other boundary conditions are also imposed. The temperature distribution on the plate equalizes over

time, according to the well-known differential equation describing heat flow:

$$\frac{\partial u}{\partial t} = \triangle u, \tag{23}$$

where $u(\cdot, t)$ is the temperature distribution on the plate at time t. As t increases, $u(\cdot, t)$ represents the signal at increasingly coarse scale (more blurring). If the initial temperature distribution is a scalar-valued function f on $\mathbb{R}^2$, the scale space of f is a scalar-valued function u on the product space $\mathbb{R}^2 \times \mathbb{R}^+$.

The operator $\triangle$ is the Laplacian; in $\mathbb{R}^2(\mathbf{x} = (x, y))$ the standard Laplacian is simply

$$\triangle = \frac{\partial^2}{\partial x^2} + \frac{\partial^2}{\partial y^2}. \tag{24}$$

This operator on functions $f \in L^2(\mathbb{R}^2)$ also extends to an operator on scale-spaces $u \in L^2(\mathbb{R}^2 \times \mathbb{R}^+)$:

$$(\triangle u)(x, y, t) = (\triangle u_t)(x, y), \tag{25}$$

where u_t is a restriction of u to a plane in t, given by $u_t(x, y) = u(x, y, t)$.

The solution to the heat equation, with initial temperature distribution $f(\mathbf{x}) \in L^2(\mathbb{R}^2)$, is

$$u(\mathbf{x}, t) = f(\mathbf{x}) \frac{1}{\sqrt{2\pi}t} e^{-\frac{|\mathbf{x}|^2}{t^2}}. \tag{26}$$

This solution is the classical linear scale space, or Gaussian blurring (see Equation 13). The standard deviation of the Gaussian kernel used for blurring can be related to the time parameter by the variable substitution $t = 2\sigma^2$.

When the domain of the signal f is a bounded region of $\mathbb{R}^2$, the solution of the heat equation depends on conditions placed at the boundary of the domain. There are a variety of reasonable choices of boundary condition: for example, filling the plane outside the region with zero, or filling the plane by extending the image periodically, or using Neumann boundary conditions, which state that no image energy should enter or leave the region.

A similar approach to scale space can be made when the domain of the signal f is generalized from $\mathbb{R}^2$ to a general Riemannian manifold $\mathcal{M}$ with metric tensor $\mathbf{g}$. The Laplacian operator generalizes to an operator on $L^2(\mathcal{M})$, and the heat equation is the same. The signal $f \in L^2(\mathcal{M})$ is the initial temperature distribution on the manifold $\mathcal{M}$. If the manifold has a boundary, then boundary conditions need to be imposed to guarantee a unique solution to the heat equation. The solution to the heat equation is a function $u \in L^2(\mathcal{M} \times \mathbb{R}^+)$ which represents the temperature at each point on the manifold at each point in time.

A manifold embedded in Euclidean space inherits a metric tensor from the embedding space; this is the Riemannian metric tensor. The Laplacian with the Riemannian metric tensor is the Laplace-Beltrami operator; it is "coordinate-free" in that it does not depend on any parameterization of the manifold but only on the local geometry of the manifold. Chung et al. have used discrete approximations to the Laplace-Beltrami operator for smoothing on the cortical surface of the brain [Chung et al. 2001]. Desbrun et al. show a discrete implementation of the Laplace-Beltrami operator on general triangle meshes [Desbrun et al. 1999]. The Laplacian can also be formed with an arbitrary metric tensor on the manifold $\mathcal{M}$, not just the Riemannian metric tensor. The approach I use to develop a scale space on the manifold $\mathcal{M}$ uses a diffeomorphic map from the sphere S^2 to $\mathcal{M}$. The map together with the natural metric tensor on S^2 implies a metric tensor on $\mathcal{M}$; the scale space I develop in Section 3.1.3 is a solution to the heat equation on $\mathcal{M}$ using that metric tensor. The connection between my scale space and Laplace-Beltrami smoothing is explored in Section 3.1.4.

3.1.2. Scale Space on the Sphere S^2. In this section I extend the heat-equation scale-space theory from scalar functions on Euclidean space to scalar functions on S^2. The theory in this section is from joint work with Remco Duits of the Technical University of Eindhoven in the Netherlands.

Let $f : S^2 \to \mathbb{R}$ be a function defined on S^2, the unit 2-sphere, which can be thought of as the surface of the unit ball in $\mathbb{R}^3$. S^2 can be parameterized by colatitude $\theta \in [0, \pi]$

and azimuth $\phi \in [0, 2\pi]$. With this parameterization there are coordinate singularities along the prime meridian ($\phi = 0, 2\pi$), including the north and south poles ($\theta = 0$ and $\theta = \pi$). For f to be well-defined in this parameterization, assume that $f(\theta, 0) = f(\theta, 2\pi)$ for all θ. Also assume that $f(0, \phi_1) = f(0, \phi_2)$ and $f(\pi, \phi_1) = f(\pi, \phi_2)$ for all ϕ_1, ϕ_2. The surface area element ds on S^2 is $\sin\theta \, \mathrm{d}\theta \, \mathrm{d}\phi$. Let $f \in L^2(S^2)$, i.e.,

$$||f||_2 = \int_{S^2} |f|^2 ds = \int_{\phi=0}^{2\pi} \int_{\theta=0}^{\pi} |f(\theta, \phi)|^2 \sin\theta \, \mathrm{d}\theta \, \mathrm{d}\phi < \infty$$

The Laplace operator on S^2 is

$$\triangle_{S^2} = \frac{\partial^2}{\partial\theta^2} + \frac{\cos\theta}{\sin\theta}\frac{\partial}{\partial\theta} + \frac{1}{\sin^2\theta}\frac{\partial^2}{\partial\phi^2}. \tag{27}$$

To solve the heat equation $\partial u/\partial t = \triangle u$ on S^2, I use a spectral solution, which uses eigenfunctions of the Laplacian linear operator. On S^2, the eigenfunctions of the Laplacian are a family of functions Y_l^m known as the spherical harmonics: they satisfy

$$\triangle_{S^2} Y_l^m + l(l+1) Y_l^m = 0, \tag{28}$$

where the eigenvalue corresponding to each Y_l^m is $l(l+1)$. For a proof that the spherical harmonics are eigenfunctions of the Laplace operator on S^2, see [Müller 1966].

Definition 1. *The* spherical harmonics *on S^2 are functions $Y_l^m : S^2 \to \mathbb{C}$ given by*

$$Y_l^m(\theta, \phi) = \sqrt{\frac{2l+1}{4\pi}} \sqrt{\frac{(l-m)!}{(l+m)!}} P_l^m(\cos\theta) e^{im\phi}, \tag{29}$$

where $P_l^m(x)$ is the associated Legendre polynomial.

The degree l of the spherical harmonic ranges from 0 to ∞. The order m within each degree l ranges from $-l$ to l.

The spherical harmonics $\{Y_l^m\}$ also form a complete orthonormal basis for $L^2(S^2)$ [Müller 1966], hence any $f \in L^2(S^2)$ has a *Fourier expansion* in spherical harmonics:

$$f(\theta, \phi) = \sum_{l=0}^{\infty} \sum_{m=-l}^{l} c_l^m Y_l^m(\theta, \phi), \tag{30}$$

where c_l^m are the complex coefficients of the spherical harmonics:

$$c_l^m = \int_{\phi=0}^{2\pi} \int_{\theta=0}^{\pi} f(\theta,\phi) Y_l^m(\theta,\phi) \sin\theta \, \mathrm{d}\theta \, \mathrm{d}\phi \tag{31}$$

The scale space on S^2 I propose is the spectral solution of the heat equation, using the spherical harmonics as eigenfunctions of the Laplacian.

PROPOSITION 1. *Let $f \in L^2(S^2)$, and let c_l^m be its spherical harmonic coefficients, as described above. The scale space of f I propose is $\Phi(f) : S^2 \times \mathbb{R}^+ \to \mathbb{R}$ given by*

$$\Phi(f)(\theta,\phi;t) = \sum_{l=0}^{\infty} \sum_{m=-l}^{l} e^{-l(l+1)t} c_l^m Y_l^m(\theta,\phi). \tag{32}$$

The scale parameter σ can also be used, with $t = 2\sigma^2$.

It is straightforward to check that this scale space satisfies the heat equation on S^2:

$$\frac{\partial}{\partial t}\Phi(f) = \frac{\partial}{\partial t} \sum_{l=0}^{\infty} \sum_{m=-l}^{l} e^{-l(l+1)t} c_l^m Y_l^m(\theta,\phi) \tag{33}$$

$$= \sum_{l=0}^{\infty} \sum_{m=-1}^{l} \left(\frac{\partial}{\partial t} e^{-l(l+1)t} \right) c_l^m Y_l^m(\theta,\phi) \tag{34}$$

$$= \sum_{l=0}^{\infty} \sum_{m=-1}^{l} \left(-l(l+1) e^{-l(l+1)t} \right) c_l^m Y_l^m(\theta,\phi) \tag{35}$$

$$= \sum_{l=0}^{\infty} \sum_{m=-1}^{l} e^{-l(l+1)t} c_l^m \left(-l(l+1) Y_l^m(\theta,\phi) \right) \tag{36}$$

$$= \sum_{l=0}^{\infty} \sum_{m=-1}^{l} e^{-l(l+1)t} c_l^m \left(\triangle Y_l^m(\theta,\phi) \right) \tag{37}$$

$$= \triangle \Phi(f). \tag{38}$$

3.1.3. Scale Space on the Boundary Manifold $\mathcal{M}$. Let the manifold $\mathcal{M}$ be the boundary of the object to be segmented. For 3D objects, $\mathcal{M}$ is a 2-dimensional manifold. Assume that $\mathcal{M}$ is differentiable and can be mapped diffeomorphically to the sphere S^2. Boundaries of simply connected objects generically will fit these assumptions. Let

$f \in L^2(\mathcal{M})$ be a scalar function on the manifold. For instance, f might be the image intensity at the boundary of the object.

To define this scale space on $\mathcal{M}$, I make use of the scale space on the unit sphere S^2 discussed in Section 3.1.2. Let $h : S^2 \to \mathcal{M}$ denote a diffeomorphism between the unit sphere and the object boundary. The *SPHARM* geometric representation provides one such diffeomorphism, since the parameter space of the spherical harmonics is the unit sphere. Since it is a diffeomorphism, it also has an inverse $h^{-1} : \mathcal{M} \to S^2$. I use the mapping h to define a pull-back of f onto S^2, call it $f^* : S^2 \to \mathbb{R}$, defined by $f^* = f \circ h$:

$$f^*(\theta, \phi) = f(h(\theta, \phi)). \tag{39}$$

Since f^* is a function on S^2, I can apply the scale space proposed in Section 3.1.2 to it.

The scale space on $\mathcal{M}$ I propose is $\Phi(f) : \mathcal{M} \times \mathbb{R}^+$ given by

$$\Phi(f)(s, \sigma) = \Phi(f^*)(h^{-1}(s), \sigma), \tag{40}$$

where $s \in \mathcal{M}$ and $\Phi(f^*)$ is the scale space on S^2 given in Section 3.1.2.

The shape representation chosen uses the spherical harmonics Y_l^m as an orthonormal basis for the geometry. Similarly, for image representation, the scale space uses the spherical harmonics Y_l^m as an orthonormal basis for image intensity fields on the object boundary.

The scale space defined in this way on $\mathcal{M}$ does not satisfy the heat equation on $\mathcal{M}$, but only the heat equation on S^2 via the diffeomorphic mapping $h : S^2 \to \mathcal{M}$. The next section discusses a solution of the heat equation directly on the manifold $\mathcal{M}$ and compares it to the scale space I use on $\mathcal{M}$.

3.1.4. Comparison with Laplace-Beltrami Smoothing. Just as the heat equation is used to construct scale spaces on Euclidean space and the sphere S^2, the heat equation can also be written using the Laplace-Beltrami operator on the manifold $\mathcal{M}$. Smoothing scalar functions on $\mathcal{M}$ via the scale space I proposed is equivalent to Laplace-Beltrami

smoothing on the manifold using the metric tensor which is inherited from the sphere S^2 via the diffeomorphic map h.

The Laplace-Beltrami operator is an extension of the Laplace operator to a Riemannian manifold $\mathcal{M}$, and it can be written as

$$\triangle_{\mathcal{M}} f = \sum_{i,j} \mathbf{g}^{ij} \frac{\partial^2 f}{\partial x_i \partial x_j} + \sum_{i,j,k} \mathbf{g}^{jk} \Gamma^i_{jk} \frac{\partial f}{\partial x_i},$$

where $\mathbf{g}^{ij}$ are the elements of the inverse of the Riemannian metric tensor and Γ^i_{jk} are the Christoffel symbols of the second kind.

The Christoffel symbols can be seen as "second-order" terms; without them, the Laplace-Beltrami operator has the same form as the Euclidean Laplacian, incorporating the metric tensor. If the diffeomorphism $h : S^2 \rightarrow \mathcal{M}$ used in my scale space is an isometry (distance-preserving map), then blurring using my proposed scale space on $\mathcal{M}$ produces the same result as Laplace-Beltrami smoothing.

If the manifold $\mathcal{M}$ has any nonuniformity in curvature (i.e., anything but a sphere), an isometric mapping to S^2 does not exist, but in the case of the *SPHARM* geometric representation for the manifold $\mathcal{M}$, the mapping $h : S^2 \rightarrow \mathcal{M}$ is designed to preserve area exactly and preserve angles approximately. As an approximation to an isometry, this diffeomorphism provides a metric tensor on the manifold $\mathcal{M}$ (inherited from the standard metric tensor on the sphere) which is similar to the standard metric tensor on $\mathcal{M}$.

Laplace-Beltrami smoothing typically uses the standard Riemannian metric tensor inherited from embedding in Euclidean space; hence it is coordinate-free (i.e., independent of any parameterization of $\mathcal{M}$). The Laplace operator on $\mathcal{M}$ can still be defined in general, however, with an arbitrary metric tensor $\mathbf{g}$. This metric tensor can be provided by the geometric representation of the object and need not be the same as the metric tensor inherited from the embedding.

My new scale space on $\mathcal{M}$ is a solution to the heat equation on $\mathcal{M}$, using the metric tensor inherited from the sphere via the diffeomorphic map h. To the extent that this

metric tensor approximates the standard metric tensor on $\mathcal{M}$, my scale space approximates Laplace-Beltrami smoothing on $\mathcal{M}$.

A solution to the heat equation can be approximated directly on the manifold $\mathcal{M}$ without going through the *SPHARM* representation, as is done here: the linear Laplace operator can be approximated locally via Taylor expansion in matrix form, and eigendecompositions of the Laplacian matrix can be used to form a solution much as the spherical harmonics are used on S^2. Desbrun et al. have implemented a discretization of the Laplace operator for scalar-valued functions defined on a manifold represented as a triangle-mesh [Desbrun et al. 1999]. This is also an approximation. The scale space I presented in Section 3.1.3 is a different approximation, which makes use of the parameterization (and hence metric tensor) provided by the *SPHARM* shape representation.

3.1.5. Properties of Scale Space. The preceding sections developed new scale spaces on the sphere S^2 and on the object boundary as a manifold $\mathcal{M}$ diffeomorphic to the sphere. The development approached scale space as a solution to the heat equation; however, Euclidean scale space has often been developed using an axiomatic approach. While some of the classical axioms of linear scale space do not extend easily to the non-Euclidean domains of S^2 and $\mathcal{M}$, in this section I examine some properties satisfied by the newly defined scale spaces. This is not meant to be a comprehensive set of axioms sufficient to specify uniquely my scale spaces; it is only a selection of necessary properties.

Let f denote the original scalar-valued signal (original image). Let $\Phi(f)$ denote my scale space of f, a scalar-valued function defined on the product space of the domain of f with the positive reals $\mathbb{R}^+$. A *blurred* version of f via the scale space $\Phi(f)$ is a restriction of $\Phi(f)$ to a fixed scale σ: $f_\sigma(s) = \Phi(f)(s, \sigma)$.

3.1.5.1. *Linearity.*

THEOREM 1. *The scale space $\Phi(f)$ is linear with respect to multiplication: for any scalar λ,*

$$\Phi(\lambda f)(\theta, \phi; \sigma) = \lambda \Phi(f)(\theta, \phi; \sigma). \tag{41}$$

Proof. For the S^2 case, since both f and λf are in $L^2(S^2)$, the spherical harmonic coefficients of λf are just

$$\int_{S^2} \lambda f(\theta,\phi) Y_l^m(\theta,\phi)\, \mathrm{d}s = \lambda \int_{S^2} f(\theta,\phi) Y_l^m(\theta,\phi)\, \mathrm{d}s \tag{42}$$

$$= \lambda c_l^m. \tag{43}$$

Hence the scale space of λf is

$$\Phi(\lambda f)(\theta,\phi;\sigma) = \sum_{l=0}^{\infty} \sum_{m=-l}^{l} e^{-l(l+1)\sigma} \lambda c_l^m Y_l^m(\theta,\phi) \tag{44}$$

$$= \lambda \sum_{l=0}^{\infty} \sum_{m=-l}^{l} e^{-l(l+1)\sigma} c_l^m Y_l^m(\theta,\phi) \tag{45}$$

$$= \lambda \Phi(f)(\theta,\phi;\sigma). \tag{46}$$

That the scale space on $\mathcal{M}$ is also linear with respect to multiplication follows, since $\Phi(f^*)$ is linear. □

3.1.5.2. *Shift Invariance.* Shift invariance applies only when the domain is shift invariant; even in Euclidean space, when the domain is bounded, shift invariance does not apply. On S^2, one concept of translation (shifting) is a group action on the sphere. Each point $s \in S^2$ has an associated group action $T_s : S^2 \to S^2$. Let the south pole ($\theta = 0$) be the identity group element, so each group action T_s takes the south pole to the point s, along the shortest geodesic path. There is no unique shortest geodesic to the north pole. The group action can be lifted to an operator on $L^2(S^2)$ given by:

$$T_s(f)(t) = f(T_s(t)), \qquad \forall t \in S^2, \tag{47}$$

where the T_s on the left hand side is an operator $T_s : L^2(S^2) \to L^2(S^2)$, and the T_s on the right hand side is a group action $T_s : S^2 \to S^2$. Shift invariance of a scale space on S^2 can then be phrased as

$$\Phi(T_s(f))(t;\sigma) = \Phi(f)(T_s^{-1}(t);\sigma). \tag{48}$$

The shift invariance of the scale space I propose on S^2 then depends on the shift invariance of the spherical harmonic decomposition.

3.1.5.3. *Semigroup Property.*

THEOREM 2. *The semigroup property states that blurring once with scale σ_1 and then blurring the result with scale σ_2 ("cascading") is equivalent to blurring the original function once with scale $\sigma_1 + \sigma_2$. Let*

$$f_{\sigma_1}(\theta, \phi) = \Phi(f)(\theta, \phi; \sigma_1); \tag{49}$$

then the semigroup property is

$$\Phi(f_{\sigma_1})(\theta, \phi; \sigma_2) = \Phi(f)(\theta, \phi; \sigma_1 + \sigma_2). \tag{50}$$

Proof. By the definition of Φ and the fact that the spherical harmonics form an orthonormal basis of $L^2(S^2)$, the spherical harmonic coefficients of f_{σ_1} are

$$(c_{\sigma_1})_l^m = e^{-l(l+1)\sigma_1} c_l^m, \tag{51}$$

where c_l^m are the spherical harmonic coefficients of the original signal f. Hence the "cascaded" blur of f is

$$\Phi(f_{\sigma_1})(\theta, \phi; \sigma_2) = \sum_{l=0}^{\infty} \sum_{m=-l}^{l} e^{-l(l+1)\sigma_2} (c_{\sigma_1})_l^m Y_l^m(\theta, \phi) \tag{52}$$

$$= \sum_{l=0}^{\infty} \sum_{m=-l}^{l} e^{-l(l+1)\sigma_2} e^{-l(l+1)\sigma_1} c_l^m Y_l^m(\theta, \phi) \tag{53}$$

$$= \sum_{l=0}^{\infty} \sum_{m=-l}^{l} e^{-l(l+1)(\sigma_1+\sigma_2)} c_l^m Y_l^m(\theta, \phi) \tag{54}$$

$$= \Phi(f)(\theta, \phi; \sigma_1 + \sigma_2). \tag{55}$$

The semigroup property on S^2 then extends to the scale space on $\mathcal{M}$ via the diffeomorphism h:

$$\Phi(f_{\sigma_1})(s,\sigma_2) = \Phi((f_{\sigma_1})^*)(h^{-1}(s),\sigma_2) \tag{56}$$

$$= \Phi((f^*)_{\sigma_1})(h^{-1}(s),\sigma_2) \tag{57}$$

$$= \Phi(f^*)(h^{-1}(s),\sigma_1+\sigma_2) \tag{58}$$

$$= \Phi(f)(s,\sigma_1+\sigma_2). \tag{59}$$

$(f_{\sigma_1})^*$ can be interchanged with $(f^*)_{\sigma_1}$ because h is a diffeomorphism.

□

3.1.5.4. *Convergence to f.*

THEOREM 3. *The scale space $\Phi(f)$ converges uniformly to the original signal f as scale $\sigma \to 0$:*

$$\lim_{\sigma\to 0}\Phi(f)(s,\sigma) = f(s). \tag{60}$$

Proof. On S^2 this follows from the orthogonal decomposition of f by the spherical harmonics as complete orthonormal basis for $L^2(S^2)$:

$$\lim_{\sigma\to 0}\Phi(f)(\theta,\phi;\sigma) = \lim_{t\to 0}\sum_{l=0}^{\infty}\sum_{m=-l}^{l} e^{-l(l+1)t}c_l^m Y_l^m(\theta,\phi) \tag{61}$$

$$= \sum_{l=0}^{\infty}\sum_{m=-l}^{l}\lim_{t\to 0} e^{-l(l+1)t}c_l^m Y_l^m(\theta,\phi) \tag{62}$$

$$= \sum_{l=0}^{\infty}\sum_{m=-l}^{l} c_l^m Y_l^m(\theta,\phi) \tag{63}$$

$$= f(\theta,\phi). \tag{64}$$

Convergence on the manifold $\mathcal{M}$ follows via the diffeomorphism. □

3.1.6. Scale Space on Profiles. In 2D images, the object boundary is a 1D curve; the collar is a 2D bent bar enveloping the boundary (Figure 3.1). In 3D images, the object

boundary is a 2D manifold $\mathcal{M}$; the collar is a 3D region of interest within the image. For my purposes I look at a collar of constant thickness extending both inward and outward from the boundary. I assume that the geometric model provides a parameterization of the 2D manifold of the boundary. What is desired is a parameterization of the full 3D collar; unfortunately few geometric models provide such a parameterization in a natural way. M-reps are one kind of geometric model that provide a parameterization of the full 3D collar; Section 5.4.4 will address a possible generalization of this method to allow application to M-rep geometry.

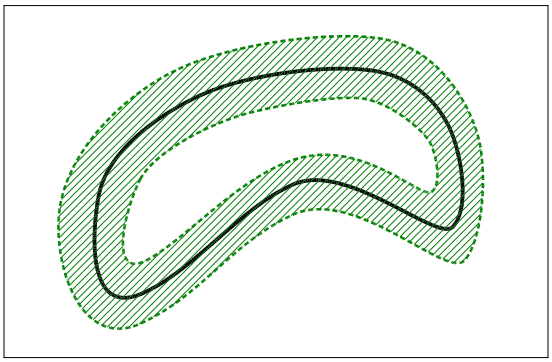

FIGURE 3.1. Illustration in 2D of the collar of interest (between dotted green curves) about the object boundary (solid black). This is the region from which profiles are extracted.

In my implementation, I choose a geometric representation based on spherical harmonics, which provides a parameterization of the 2D manifold of the object boundary in terms of a parameterization of the unit sphere S^2. A traditional triangle mesh representation of the boundary could also be used. The *SPHARM* representation, described in Section 2.2, also analytically provides normal vectors to the boundary.

To extend the parameterization from the 2D manifold $\mathcal{M}$ of the object boundary to the 3D collar about the boundary, I use straight one-dimensional *profiles* extending normal to the object boundary. Thus I have a geometry-dependent mapping

$$\mathcal{M} \times [-1, 1] \rightarrow \Omega : (u, \tau) \mapsto \mathbf{x},$$

where u parameterizes the object boundary, τ specifies distance normal to the boundary, and $\mathbf{x}$ represents a location in the original (x, y, z) image coordinates. Since $\mathcal{M}$ is a 2D manifold, u is a parameter vector with two degrees of freedom. The units of τ need not be Euclidean distance, but in my implementation the sampling along each profile is uniform in Euclidean distance. This definition of profiles uses a local linear approximation to the object boundary $\mathcal{M}$ to estimate a parameterization of the entire collar about the object boundary. This is the standard profile sampling scheme used by Active Shape Models [Cootes et al. 1993] and Kelemen's *SPHARM* segmentation framework. This is what I use in my implemention as well. Where the manifold $\mathcal{M}$ has curvature, however, the straight-line profiles may cross. Possible future work could be to refine the profile sampling scheme, perhaps by a flow-field away from $\mathcal{M}$ along the distance map. If the object geometry is represented by m-reps [Pizer et al. 2003] instead of *SPHARM*s, then another parameterization can be provided of a collar about the object. Profiles from such parameterizations would no longer be straight, and might be sampled non-uniformly along their lengths.

Given a parameterization of the collar about the object boundary, I sample a *profile image* I from the original image on profiles across the object boundary. With the *SPHARM* geometric representation, the parameter space of the spherical harmonics is the surface of the unit sphere, S^2. Hence a natural space for the normalized coordinate system is

$$(\theta, \phi, \tau) \in S^2 \times [-1, 1]$$

where (θ, ϕ) parameterize the sphere and τ indicates distance normal to the boundary. This is a spherical shell with thickness; it represents an idealized collar about the object boundary. Normals on the sphere S^2 map to normals on the object boundary $\mathcal{M}$; the collar has constant thickness in the image space.

The profile image I is a scalar function on the normalized coordinate space:

$$I : \mathcal{M} \times [-1, 1] \rightarrow \mathbb{R}.$$

For my purposes, I can also consider the profile image I as a tuple-valued function defined on the surface of the unit sphere:

$$I : S^2 \rightarrow L^2[-1, 1],$$

where the value of I at each (θ, ϕ) on the sphere is a 1D function describing the intensity profile across the object boundary at that point. A possible extension could represent the 1D profiles via orthogonal polynomial expansion, e.g., Legendre polynomials.

A uniform sampling of the object boundary is obtained by an octahedron-based triangle subdivision of the sphere S^2. At each point on the object boundary, the image is sampled evenly along a straight line normal to the boundary, producing an image profile. The first image in Figure 3.2 shows 512 profiles taken around one caudate from the training set. The 1D ordering of the profiles represents a certain traversal of the 2D surface of the object; adjacent profiles in this visualization are not necessarily adjacent on the surface. This visualization does illustrate the complex image appearance at the boundary: some profiles show the border with the ventricle (black in T1-weighted MRI), some show a border with white matter, and some show no contrast at all with tissue outside the caudate.

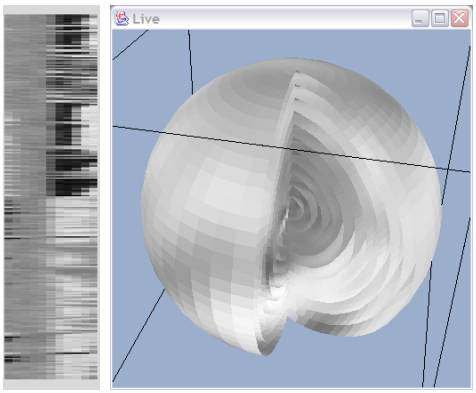

FIGURE 3.2. Intensity profiles from the boundary of a single caudate. At left is a linear visualization of the profiles: the left half is inside the caudate; the right half is outside. At right is an "onionskin" visualization of the profiles mapped onto concentric spheres. Each sphere represents sampled intensities at a fixed distance away from the boundary, from -5mm to +5mm, with 1mm spacing.

The right image in Figure 3.2 shows a different visualization of the same profiles, mapped onto concentric spheres. The diffeomorphic mapping of the object to the sphere S^2 provided by the shape representation is used to map each level of the profiles to a sphere. The outermost sphere represents intensities sampled from an "onionskin" +5mm outside the object boundary. Each profile is 11 samples long, so there are 11 concentric spheres in the visualization. The uniform grey matter interior of the caudate can be seen on the interior spheres.

Figure 3.3 shows one particular "onionskin" at +5mm outside one particular caudate. The image intensities are texture-mapped back onto the geometry of the caudate at the boundary, as defined by the manual expert segmentation. Four levels of scale are shown to illustrate the scale space along the boundary.

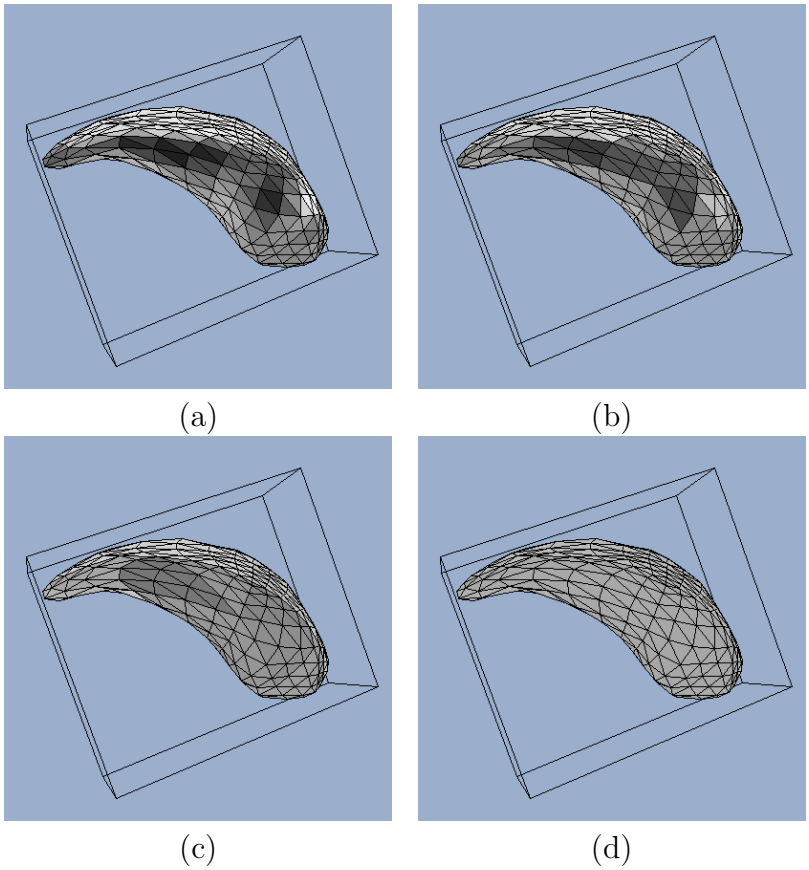

FIGURE 3.3. Visualization of an "onionskin" sampled at +5mm outside the caudate, texture-mapped back onto the original caudate geometry (manual expert segmentation). Shown are four scale levels from the scale space, fine to coarse. The region abutting the lateral ventricle (see Figure 1.4) is seen as a medium-large scale dark area.

3.2. The Probabilistic Model on the Profile Scale Space

The preceding section defined a *profile scale space*, a scale space on a set of profiles taken about the boundary of a single geometric object in a single image. In this section I define my Bayesian image match model as a particular probability distribution on the profile scale space.

A Bayesian image match model for deformable-models segmentation is a probability distribution on features obtained from an image, given an instance of object geometry. Image match models are trained by extracting features from a population of training images that each have corresponding object geometry from expert segmentation.

My project uses a population of 114 magnetic resonance images (MRIs) of the human brain with corresponding manual segmentations of the caudate provided by human expert raters (see Section 4.2 for more details). My image match model is trained by first building a profile scale space for each image in the training population, using geometry from the corresponding manual segmentation. Each profile scale space in the training population is then sampled to obtain a collection of profiles blurred at multiple scales; this is described in Section 3.2.1 The blurred profiles are used to train the Markov Random Field (MRF) probability distribution that defines my image match model; Section 3.2.2 discusses this MRF model.

There may be other ways to define a probability distribution on a scale space; the approach I choose is inspired by multiresolution Markov Random Fields on 2D images [Bouman and Shapiro 1994, Willsky 2002].

3.2.1. Sampling the Profile Scale Space. A profile scale space $\Phi(f)$ as described in Section 3.1 can be seen as a tuple-valued function on the domain $S^2 \times \mathbb{R}^+$. At each point (ϕ, θ) in the parameter space S^2 of the *SPHARM* geometric representation of the object, for each scale σ in $\mathbb{R}^+$, the tuple given by $\Phi(f)(\phi, \theta; \sigma)$ represents a blurred profile of the object boundary at the point mapped to by (ϕ, θ), blurred at scale σ. The profile scale space is continuous, but in order to develop a probabilistic model I sample from the continuous profile scale space at a discrete set of (ϕ, θ) and σ. Following the concept of

the Gaussian pyramid for images in Euclidean space, I sample the parameter space S^2 more sparsely at coarser scales and more densely at finer scales.

My sampling of S^2 is derived from a triangular tessellation of the sphere. I start with an octahedron; the center of each of the eight triangles corresponds to a coarse-scale blurred profile. A recursive triangle subdivision provides denser samplings of the sphere, at which finer-scale profiles are sampled from the continuous profile scale space. I use 512 profiles at the finest scale, 128 profiles at a coarser scale, 32 profiles at a yet coarser scale, and 8 profiles at the top level of scale. The recursive triangle subdivision also provides parent-child relationships between profiles at adjacent scales. A schematic of the sampling scheme is illustrated in Figure 3.4(a). Each node in the tree graph (call it G) represents a single profile sampled from the profile scale space. The node at the top of the tree represents a single coarse-scale profile summarizing an eighth of the boundary. The figure only shows a portion of the sampling for clarity, but the hierarchical sampling is on the whole sphere S^2.

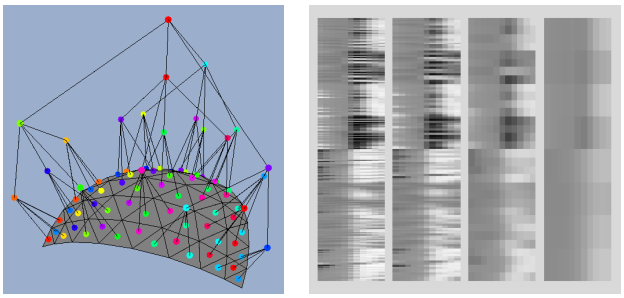

(a) (b)

FIGURE 3.4. (a) Visualization of the coarse-to-fine sampling of the profile scale space. Each node in the tree G represents a single profile sampled from the profile scale space. Distance away from the grey sphere indicates coarser scale in the scale space. (b) Average profiles across the training population, at four scales, fine to coarse.

These blurred profiles are calculated for each object in the training population. To visualize the sampled profiles, Figure 3.4(b) shows the mean profiles at multiple scales, where the mean is taken at corresponding locations over the training population. Correspondence is established via the spherical harmonic parameterization [Kelemen et al.

1999]. In this visualization the ordering of the profiles from top to bottom represents a particular traversal of the 2D manifold of the object boundary; this blurring is not the same as a simple y-axis blur on the profiles.

Having described the pyramidal sampling of the profile scale space, in the next section I describe a Markov Random Field probabilistic model on the sampled profile scale space.

3.2.2. Markov Random Field Model on Derived Feature Vectors. A Markov Random Field (MRF) [Geman and Geman 1984] is a common choice for trees of statistical features such as represented in Figure 3.4. The major components of a Markov Random Field model that need to be specified are the neighborhood relations and the local clique potentials. The neighborhood relations define which pairs of nodes have explicitly modeled covariance; the local clique potentials specify that covariance between pairs of neighbors.

In my MRF model the neighborhood relations are given by the parent-child links in the tree: the neighborhood of each node in the tree is defined to be the set containing the node's parent and all of the node's children. These neighborhood relations in the bidirectional graph G in Figure 3.4 imply a set of cliques, fully-connected subsets of the graph. There are two types of cliques in the tree graph, singletons and parent-child pairs. These two types of cliques are illustrated in the sketch in Figure 3.5. Let $\{u_i\}$ represent the nodes in the tree (profiles sampled from the profile scale space), indexed by i. Let $\mathrm{par}(i)$ represent the index of the parent of node i.

The eight profiles at the coarsest scale are included unchanged as features. This is analogous to the classical Laplacian image pyramid [Burt and Adelson 1983] in Euclidean space. Each scale-residual profile is then modeled as a sample from a Gaussian probability distribution of dimension equal to the number of image samples along the length of the profile. Using profiles 11 samples long there are (512+128+32+8) Gaussian distributions, each 11-dimensional. Figure 3.6 shows the mean of each of these Gaussian distributions. In the Markov Random Field framework, the Gaussian distributions are interpreted as local clique potentials, as described in the next section. The local Mahalanobis distances

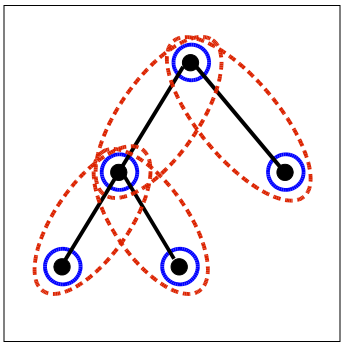

FIGURE 3.5. Sketch of two types of cliques in a Markov Random Field graph. Singletons (circles) are cliques of only one node. Parent-child pairs (dashed ovals) are cliques of two nodes.

are summed to produce a global image match. Compare this model with a single-scale profile model akin to that used in Active Shape Models, which would have 512 Gaussians, each 11-dimensional. Compare also to Active Appearance Models, which would have a single very high-dimensional Gaussian rather than many low-dimensional Gaussians.

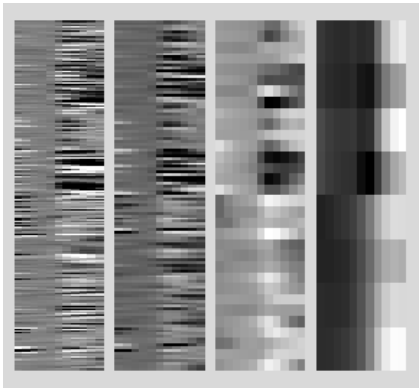

FIGURE 3.6. Means of scale residuals from the profile scale space. Four scale levels are shown, fine to coarse (the coarsest level of scale does not represent scale residuals but original blurred profiles). Each row in each scale level represents the mean of a local Gaussian potential.

Thus the multiscale features used are samples from a Laplacian pyramid on the object boundary $\mathcal{M}$, akin to Laplacian basis functions, except that the domain is no longer Euclidean space but the manifold of the object boundary. Rather than a Laplacian basis, it is possible to use an orthogonal set of wavelet bases [Van de Wouwer 1998]; this has

been done by others in Euclidean space to produce wavelet-domain hidden Markov models [Choi and Baraniuk 2001, Liu et al. 1999]. In this domain spherical wavelets [Schröder and Sweldens 1995] may be appropriate.

3.2.2.1. *Local Clique Potentials.* To specify the MRF model, local potential functions need to be defined for each clique in the tree of features. For the singleton cliques the local potentials are in the form $Vs_i(u_i)$. For the singletons at the coarsest level of scale (8 profiles in my sampling) I choose to measure the Mahalanobis distance in a multidimensional Gaussian:

$$\tilde{V}_i(u_i) = \text{Mahalanobis}_{\tilde{\mu}_i,\tilde{\Sigma}_i}(u_i) \tag{65}$$

$$= (u_i - \tilde{\mu}_i)^T \tilde{\Sigma}_i (u_i - \tilde{\mu}_i). \tag{66}$$

The finer-scale singeltons are modeled with constant potentials and do not contribute directly to the overall probability distribution. The tilde superscripts denote parameters related to the singleton cliques.

For parent-child pairs $(u_i, u_{\text{par}(i)})$ I define the clique potential to be a Mahalanobis distance on the difference or residual between a node and its parent:

$$V_i(u_i, u_{\text{par}(i)}) = \text{Mahalanobis}_{\mu_i,\Sigma_i}(u_i - u_{\text{par}(i)}) \tag{67}$$

$$= \left(u_i - u_{\text{par}(i)} - \mu_i\right)^T \Sigma_i \left(u_i - u_{\text{par}(i)} - \mu_i\right). \tag{68}$$

I define the local clique potentials using Gaussians, but other choices of clique potential could also be used.

3.2.2.2. *Markov Assumption.* The Markov assumption on the derived feature vectors $\mathbf{u}$ with respect to the tree G is that the conditional likelihood of any feature vector given all the other feature vectors in the tree is the same as the conditional likelihood of that feature vector given only its parent:

$$p\left(u_i | \{u_j : j \neq i\}\right) = p\left(u_i | u_{\text{par}(i)}\right).$$

3.2.2.3. *Gibbs formulation.* According to the Hammersley-Clifford theorem [Hammersley and Clifford 1972, Geman and Geman 1984] making the Markov assumption on $\mathbf{u}$ with respect to the tree G is equivalent to modeling the distribution $p(\mathbf{u})$ with a Gibbs distribution:

$$p(\mathbf{u}) = \frac{1}{Z} e^{-\frac{1}{T}\left(\sum_i \tilde{V}_i + \sum_i V_i\right)}, \tag{69}$$

where Z is a normalization factor (partition function) and T is a constant (temperature). This defines a probability distribution on the feature vectors $\mathbf{u} = \{u_i\}$ derived from the profile image I. The profile image samples the image relative to the boundary given by the geometric shape representation. The likelihood $p(\mathbf{u})$ defines the image match $p(I|m)$, how well a deformed shape model matches the image.

Compare this formulation of $p(I|m)$ to that used by the classical single-scale profile model:

$$p'(I|m) = \frac{1}{Z'} e^{-\sum_j {V'}_j}, \tag{70}$$

where the index j iterates over all profiles around the boundary, and the local Gaussian potentials ${V'}_j$ are on individual profiles, estimated by conditional maximum likelihood estimation. Z' is the normalization factor for the single-scale image match.

Both my multiscale profile model and the single-scale profile model make assumptions on the interdependence between profiles. In the single-scale model, each profile is assumed to be independent of all other profiles: the overall image match is simply the product of the Gaussian likelihoods for individual profiles. In my multiscale profile model, dependence between profiles is modeled. The Markov assumption I use states that the interdependence of profiles is only through the parents in scale in the graph G.

3.2.3. Parameter Estimation. The parameters in the Gibbs distribution $p(\mathbf{u})$ are the vectors and matrices for each of the Gaussian local clique potentials: $\tilde{\mu}_i, \tilde{\Sigma}_i, \mu_i, \Sigma_i$ for each clique. The "temperature" T is a user-adjustable parameter. The normalization factor (partition function) Z can be derived from the $\tilde{\Sigma}_i$ and Σ_i.

Since each of the local clique potentials is merely a quadratic, a conditional maximum likelihood estimate of each $(\tilde{\mu}_i, \tilde{\Sigma}_i)$ and (μ_i, Σ_i) is straightforward. From each segmented image in the training population the profile scale space is built and sampled to get the feature vectors $\{u_i^n\}$, where i indexes position and scale in the scale space and $n \in [1, N]$ indexes the case number in the training population. The scale residuals are $\{u_i^n - u_{\text{par}(i)}^n\}$. Then the conditional maximum likelihood estimates of the parameters in the local Gaussian potentials can be made in the usual way, e.g., via singular value decomposition:

$$\tilde{\mu}_i = \frac{1}{N} \sum_{n=1} N u_i^n, \tag{71}$$

$$\mu_i = \frac{1}{N} \sum_{n=1} N u_i^n - u_{\text{par}(i)}^n, \tag{72}$$

$$\tilde{\Sigma}_i(n_1, n_2) = \left(u_i^{n_1} - \tilde{\mu}_i\right)^T \left(u_i^{n_2} - \tilde{\mu}_i\right), \tag{73}$$

$$\Sigma_i(n_1, n_2) = \left(u_i^{n_1} - u_{\text{par}(i)}^{n_1} - \mu_i\right)^T \left(u_i^{n_2} - u_{\text{par}(i)}^{n_2} - \mu_i\right). \tag{74}$$

$\tilde{\Sigma}_i(n_1, n_2)$ denotes the (n_1, n_2)-th element of the covariance matrix $\tilde{\Sigma}_i$.

However, the true maximum likelihood estimate of the parameters requires an estimate of all the $(\tilde{\mu}_i, \tilde{\Sigma}_i)$ simultaneously. A computationally expensive iterative method of finding the true maximum likelihood estimate is the Monte Carlo Markov Chain (MCMC) [Doucet 1998] method, which converges in the limit. The conditional maximum likelihood estimate, however, is a reasonable estimate that is easily computed and can be used as an intialization for further MCMC refinement if desired.

CHAPTER 4

Experimental Results

Chapter 3 defined the new multiscale profile model that I use for image match in Bayesian segmentation. In this chapter I describe validation experiments which measure the quality and efficacy of my multiscale profile model in comparison with the classical single-scale profile model used in Active Shape Models and Kelemen's *SPHARM* segmentation framework. Section 4.1 describes the *Mathematica* implementation I have written of both my new multiscale profile model and the classical single-scale profile model. A segmentation framework has also been implemented to optimize the image match from the profile models together with a shape prior. Section 4.2 discusses the 114 magnetic resonance image (MRI) datasets I use and their associated high-quality manual segmentations of the caudate. These are the images I use for training my profile model, validating it, and evaluating its efficacy in segmentation. In Section 4.3.1 my multiscale profile model is compared against the single-scale profile model in the areas of model generalizability, specificity, and variance. Section 4.3.2 evaluates the performance of both profile models in segmentation, using the same shape prior for both image match models.

4.1. Implementation

A complete model-building and segmentation framework to test the methods presented in Chapter 3 has been written in *Mathematica*, as a proof-of-concept implementation. *Mathematica* notebooks have been written to build the *SPHARM* statistical shape model and my new multiscale profile model. Notebooks have also been provided to use these models in segmentation. A single-scale profile model in the fashion of Kelemen's

SPHARM segmentation framework has also been provided for comparison. The segmentation process uses exactly the same shape prior with both multiscale and single-scale profile models, to facilitate comparison of the two image match models.

The implementation expects as input the population of training images in the Hierarchical Data Format (HDF) file format. External C programs are needed to preprocess the binary segmentation label-map images, extracting a surface net representation of the segmentation, as well as the area-preserving parameterization in S^2 of the object surface. From the `*.net` surface net files and the `*.par` parameterizations of the object surface, the *Mathematica* notebooks can extract *SPHARM* representations of the segmented objects.

The package is a set of over a dozen *Mathematica* 5.0 notebooks, including the following:

`ExtractSpharm.nb`: Calculates *SPHARM* geometric representations of the segmented objects from `*.net` and `*.par` files.

`ShapeModel.nb`: Builds the *SPHARM* statistical shape model.

`SampleImage.nb`: Samples profiles from the training images relative to their segmentations.

`SmoothTextures.nb`: Builds the profile scale space as defined in Section 3.1.6.

`ProfileModel.nb`: Builds the new multiscale profile model for statistical image match.

`ProfileModelASM.nb`: Builds the classical single-scale profile model, for comparison.

`Segmenter.nb`: Segments a target image using the *SPHARM* statistical shape prior and either my new multiscale image match or the classical single-scale image match.

More detailed implementation notes can be found in the *Mathematica* notebooks, which allow both documentation and implementation to be interwoven in a logical outline format.

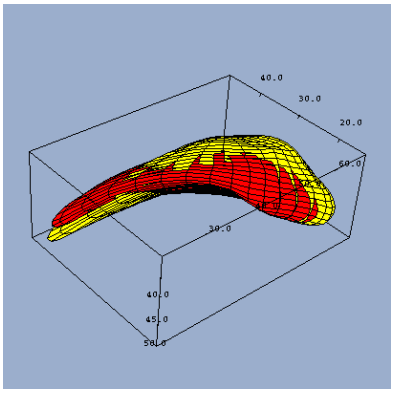

FIGURE 4.1. Illustration of the deformable segmentation process, showing initialization (mean shape) in red and manual "gold standard" segmentation in yellow.

4.1.1. Single-scale Profile Model. The single-scale profile model is implemented in the notebooks `SampleImage.nb` and `ProfileModelASM.nb`. Each training image has an associated *SPHARM* shape representing its manual segmentation (see Section 4.2 below for more details). Subroutines in `SampleImage.nb` sample the image along 512 equally-spaced straight-line profiles normal to the object boundary; each profile has 11 samples along its length at 1mm spacing. Half of the samples are inside, and half are outside the object. This is done for each of the images in the training population; the profiles are then saved to disk.

The notebook `ProfileModelASM.nb` produces for each of the 512 profiles a separate 11-dimensional Gaussian model at that location on the object boundary. The overall image match across all profiles is defined to be the product of all the 512 individual Gaussian likelihoods, as described in Section 3.2.2.3.

The single-scale profile model is designed to be modular with the new multiscale profile model, such that in segmentation a simple "switch" toggles between the two profile models, while using the same shape prior.

4.1.2. Multiscale extension. To implement my new multiscale profile model, for each training image, I start from the 512 profiles of length 11 obtained by `SampleImage.nb`, and treat them as 11 different textures (scalar-valued functions) on the corresponding *SPHARM* shape. The *SPHARM* shape representation allows one to think of the 11

"onionskin" textures as scalar-valued functions on the sphere, the parameter space of the *SPHARM*s. To construct the scale space as defined in Section 3.1.2, I use the same subroutines that were used to extract coefficients of spherical harmonics for the shape representation; they are reused to obtain coefficients of spherical harmonics for representation of the image profiles, one "onionskin" at a time. Reconstruction of a blurred version of a texture is then simply an interpolation with spherical harmonics, modulated by the $e^{-l(l+1)t}$ factor as discussed in Section 3.1.2.

In my implementation I sample the profile scale space at four levels of scale, following a coarse-to-fine pyramidal sampling from the octahedron-based triangle subdivision of the sphere. At the finest level of scale there are 512 profiles; the coarser levels have 128, 32, and finally 8 profiles. Thus at the coarsest level of scale each profile sampled from the scale space represents one octant of the object boundary. The feature vectors used in the Markov Random Field probabilistic model are the scale residuals $\{u_i - u_{\mathrm{par}(i)}\}$; these are obtained simply enough, since the triangle subdivision of the sphere allows me to keep track of "parent" triangles and hence "parent" nodes in the scale space. The 8 profiles at the top coarsest level of scale are used as-is.

Conditional maximum-likelihood parameter estimation is performed for each of the 512+128+32+8 local potentials, by calculating mean and covariance matrices on the scale-residual profiles (in the case of the 3 finer scales) or on the blurred profiles (in the case of the top level of scale). The normalization factor Z ("partition function") in the Gibbs distribution (see Section 3.2.2.3) is not explicitly calculated. The optimization for segmentation, described in the next section, minimizes $-\log p(I|m)$. Since $p(I|m)$ is in the form of a Gibbs distribution,

$$-\log p(I|m) = -\log \frac{1}{Z} e^{-\frac{1}{T}\left(\sum_i \tilde{V}_i + \sum_i V_i\right)} \tag{75}$$

$$= \log Z + \frac{1}{T}\left(\sum_i \tilde{V}_i + \sum_i V_i\right). \tag{76}$$

The $\log Z$ term is fixed once the model has been trained, so it can be ignored in the optimization process. The $1/T$ factor can be absorbed in a user-controlled parameter determining the relative weights of the shape prior versus the image match.

4.1.3. Shape Prior. The shape prior I use is a Gaussian distribution on the spherical harmonic coefficients of shape, the same as that used in Kelemen's *SPHARM* segmentation framework:

$$p(m) = N(\mu_c, \Sigma_c)(\mathbf{c}) \tag{77}$$

$$= \frac{1}{Z_c} e^{-\frac{1}{2}(\mathbf{c}-\mu_c)^T \Sigma_c (\mathbf{c}-\mu_c)}, \tag{78}$$

where $N(\mu_c, \Sigma_c)(\mathbf{c})$ represents the Gaussian likelihood of the coefficient set $\mathbf{c}$ in the multidimensional normal distribution with mean shape μ_c and covariance matrix Σ_c. Z_c is a normalization factor. The parameters μ_c and Σ_c of the Gaussian distribution are trained on a training set of shapes from manual segmentation, normalized for translation and rotation.

4.1.4. Optimization. With the probabilistic models for shape prior and image match likelihood defined Bayesian segmentation is simply optimization of the posterior, equivalent to minimization of the sum $-\log p(m) - \log p(I|m)$. The optimization is easy to specify but difficult to implement in a robust and efficient way. *Mathematica* provides a number of sophisticated optimization libraries, including non-linear optimization via genetic algorithms (`DifferentialEvolution`), simplex (`NelderMead`), and randomized local search (`RandomSearch`). During development of my implementation various optimization techniques were tried, but the numerous program parameters in the non-linear techniques proved too complex to fine-tune to gain an understanding of what the optimization was doing "behind the scenes". For the segmentation results shown in Section 4.3.2 simple conjugate-gradient optimization (`FindMinimum`) is used. Initialization is always at the mean shape; mean translation and rotation is also recorded and used for pose initialization. A hyper-parameter β modulates the log-likelihood of image match:

$\beta \log p(I|m)$. This allows the user to shift the weighting between shape prior and image match. The default value of β is 0.05 and is fixed for both multiscale and single-scale image match models.

Since the optimization is searching for the best shape to fit the image, the search space over which optimization is performed is the shape space. The shape space is limited to the 12 largest eigenmodes of deformation. The geometric representation also allows unrestricted motion of the object in translation and rotation; the total dimension of the search space is 18. Thus the search space is not too large, but each iteration takes about 6-7 seconds on a 2GHz Intel Xeon server with 2GB of RAM. About half the time is spent building and sampling from the profile scale space.

4.2. Image Datasets and Manual Segmentations

This project is fortunate in that access is provided to an unusually large and high-quality set of segmented images. A total of 115 high-resolution images with high-quality expert manual segmentations of the caudate have been provided by two projects in the Psychiatry department at UNC: a longitudinal study in autism (NIH RO1 MH61696) and a longitudinal study in Fragile X syndrome (NIMH MH 64580); Dr. Joseph Piven is the principal investigator of both. Manual segmentations are by Michael Graves, with protocol development by Rachel Gimpel and Heather Cody Hazlett. Image processing is by Rachel Gimpel.

The grayscale images are mostly coronal IRPrep T1-weighted MRI, with voxel sizes of $0.78125 \times 0.78125 \times 1.5mm^3$ and resolution $256 \times 256 \times 124$. Each was then rigidly aligned to a Talairach coordinate system via AC/PC landmarks and resampled to $1 \times 1 \times 1mm^3$ voxel spacing. For processing efficiency I cropped a fixed region of interest about the caudate and converted to the HDF image file format for import into *Mathematica*. No intensity normalization was performed on the images; the MR images in this study are quite consistent in global brightness and contrast. My multiscale profile model isolates the global brightness level (i.e., additive constant) in the top (coarsest) level of the pyramid

sampled from the profile scale space. Since the features at finer levels of scale are all scale residuals, they are inherently normalized for global brightness. Contrast (i.e., a multiplicative constant) which is consistent across the population is modeled in the local covariance matrices.

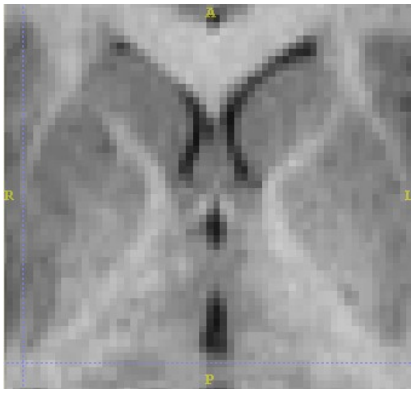

FIGURE 4.2. Cropped axial view of the caudate in T1-weighted MRI. The dark butterfly shape in the upper center of the image is the lateral ventricles; the left and right caudates are the two gray blobby structures bounded by the "wings" of the butterfly.

For the Psychiatry projects the manual raters spent a number of months developing a very careful protocol for manual segmentation of the caudate; as a result, the manual "gold-standard" segmentations are of high quality. A subset of the images was manually segmented repeatedly; I use these repeated segmentations to evaluate inter-rater and intra-rater reliability in the manual segmentation. Five datasets were chosen from the pool of images, replicated three times, and randomly ordered. Two experts then manually segmented each of the 15 3D images, resulting in a total of six segmentations for each of the five datasets. The self-consistency of each expert can be evaluated, since each expert segmented each image three times. The two experts can also be compared, to see if they do the same job. It is rare in medical image analysis to have these figures for the manual raters; it allows evaluation of the reliability of my automatic segmentation method in the context of the reliability of manual experts.

The manual segmentation reliability study will be discussed again in the segmentation tests in Section 4.3.2. The next section first evaluates my multiscale profile model on its

own as a probabilistic model, separate from a segmentation framework; evaluation of my profile model for use in segmentation is discussed later.

4.3. Validation

In this section I compare my new multiscale profile model to a standard single-scale profile model, akin to that used by Active Shape Models or the spherical harmonics framework of [Kelemen et al. 1999]. Validation is done in two parts: first, the profile model is be evaluated on its own as a probabilistic model – how well does the model fit the training data? Secondly, the profile model can be evaluated for its utility in segmentation – does it contribute towards automatic segmentations that are closer to the manual segmentations?

4.3.1. Evaluation of the Probabilistic Model. An image match model can be evaluated as a probabilistic model on a high-dimensional feature space: given a training population, one can ask how well the model fits the training population. Two aspects of model quality that are of interest are *generalizability* and *specificity*. Generalizability is a measure of how well the model generalizes to a sample point outside the training population. Specificity is a measure of how tightly the model fits around the training population. I evaluate generalizability by using a sample from the random variable which is not part of the training population. The likelihood of that sample in the probability distribution yields a measure of generalizability. To evaluate specificity, I use a random sample generated from the probability distribution. The distance from that generated sample to the nearest sample in the training population yields a measure of specificity. This requires a distance metric between samples of the random variable. In Section 4.3.1.3 I also evaluate the variance of the single-scale and multiscale profile models.

Figure 4.3 illustrates generalizability and specificity using a toy example in a 1D feature space. The x axis indicates the value of a single random variable; round dots are values of the random variable in a training population. The y axis indicates probability density in the model; the probability distribution is shown as a curve. The "X" indicates the value of a sample which was not included in the training, but which comes from the same random variable and ought to have a high likelihood in the model. Figure 4.3(a) shows a model that is quite general but not very specific. Although it gives a high

likelihood to the left-out sample point "X", the model is likely to generate samples which are very far from the training population. Figure 4.3(b) illustrates the other extreme: the model is very specific to the training population (generated samples are likely to be very near the training population), but the model does not generalize well to the sample point "X", which ought to have a high likelihood. Figure 4.3(c) shows one possible model that strikes a balance between generalizability and specificity. The models in these sketches were in fact generated by Gaussian Parzen windowing with window sizes of $\sigma = 0.8, 0.02, 0.09$.

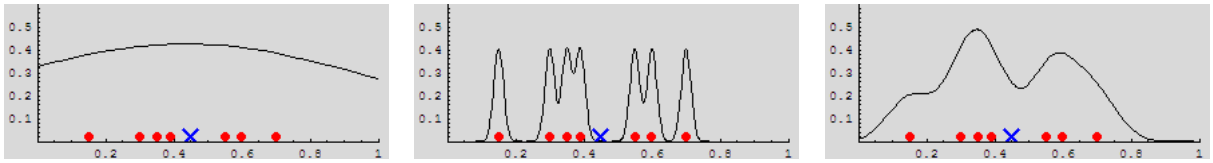

(a) (b) (c)

FIGURE 4.3. Illustration of generalizability and specificity in model quality, using a toy example in 1D. x axis is the value of the random variable; y axis is probability. (a) The model (curve) is very general but not very specific to the training population (round dots). (b) The model is very specific to the training, but does not generalize well to the new sample point marked with an "X". (c) The model balances generalizability with specificity.

Styner et al have used the concepts of generalizability and specificity in comparing various definitions of point-to-point correspondence in shape representation [Styner et al. 2003]. I also examine variance in the image match models, since the models use Gaussian distributions.

I examine the quality of the model as a function of training population size; the claim is that my new multiscale profile model requires fewer training samples to obtain a "good" model than the classical single-scale profile model does. There is a fixed total of 114 segmented images, from which profiles can be extracted relative to the manually segmented objects. I consider five sizes of training populations, using 10%, 30%, 50%, 70%, and 90% of the total pool of images to train the model. For each size I randomly selected training populations five times from the total pool, training a model on each of

those populations. Thus the model was trained a total of 25 times on different populations. For each choice of training population the remaining images from the pool of 114 can be used as test images. This is a series of *jack-knife* tests, splitting the total pool at random into *training* and *testing* populations.

4.3.1.1. *Generalizability.* To evaluate generalizability, for each split of training versus testing populations, the model is trained on the training population and the likelihood of each sample in the testing population is evaluated. If the model is generalizable, then the generated samples should have high likelihood in the model. The results can be considered for the various sizes of training population.

Figure 4.4 shows the likelihood of samples from the testing populations, for various sizes of training population. Each column of dots represents one choice of test vs. training and hence one instance of a trained model. The columns are clustered according to size of training population, at 10%, 30%, 50%, 70%, and 90% of the total of 114 segmented images. The vertical axis indicates the negative log-likelihood of each of 5 test samples in each of the trained instances of the model; lower values are increased likelihood and better generalizability of the model.

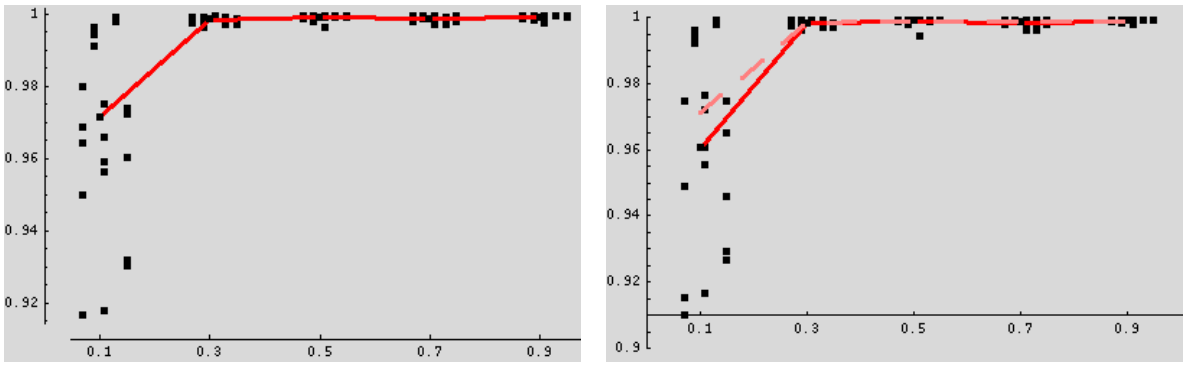

(a) (b)

FIGURE 4.4. Generalizability of (a) the multiscale profile model and (b) the single-scale profile model, as a function of training population size. Training populations are chosen of sizes 10%, 30%, 50%, 70%, and 90% of the total pool of 114. For each size, five training populations were randomly selected; the remainder were used for testing. For each trained model, the likelihood of the test samples are plotted in the vertical axis; higher values indicate better generalizability.

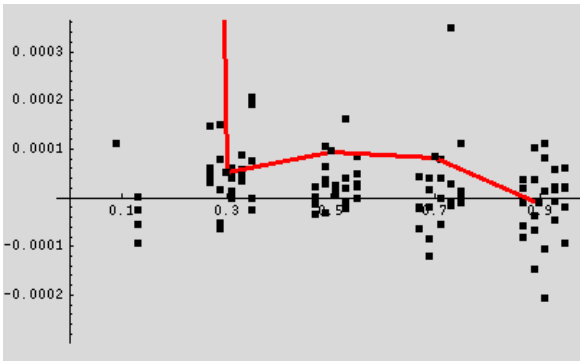

FIGURE 4.5. Pointwise difference in generalizability between multiscale model and single-scale model, when trained on the same training populations. Axes are as in Figure 4.4. The generalizability of both models on training populations of size larger than 10% does not differ significantly.

The multiscale and single-scale profile models use exactly the same training populations and test samples, so the plots in Figure 4.4 are directly comparable. The results indicate that in terms of generalizability, the two models are very similar. In both models, training with only 10% (11 images) of the total number of datasets is not advisable, since it yields very poor generalizability, as expected. Figure 4.5 shows that the difference in generalizability between multiscale and single-scale models trained on the same population is negligible for reasonable training populations of size 30% or more.

My new multiscale profile model performs about as well as the classical single-scale profile model in the area of generalizability. The next section compares the performance of these two profile models in the area of specificity, where the new model shows a significant improvement.

4.3.1.2. *Specificity.* One measure of specificity generates samples from the probability distribution and compares how close the generated sample is to the nearest object in the training population [Styner et al. 2004, Davies et al. 2003]. In the application of Styner et al. [2004] the probability distribution is on shapes, so the metric of "closeness" of two samples is for instance the mean squared-distance (MSD) between corresponding points on the object surface. In this application the probability distribution is on sets of profiles, so a reasonable metric I choose of "closeness" of two samples is the mean squared-difference in intensity of corresponding profiles. There may be other possible

metrics; the mean squared-difference may be biased by high intensity profiles due to components of variance which might be tied to the brightness level.

Using the same 25 selections of training populations used in the generalizability test, 20 sample profile sets are generated from each of the 25 profile models. Each generated profile set is compared against all the profiles in the training population; the smallest mean squared-difference (the distance to the nearest profile set) is plotted in Figure 4.6. Again, the five clusters left-to-right denote varying sizes of training population. Each cluster has five columns representing the results for five training populations of that size. The vertical axis denotes mean squared-difference in image intensity between the generated profile set and the closest profile set in the training population.

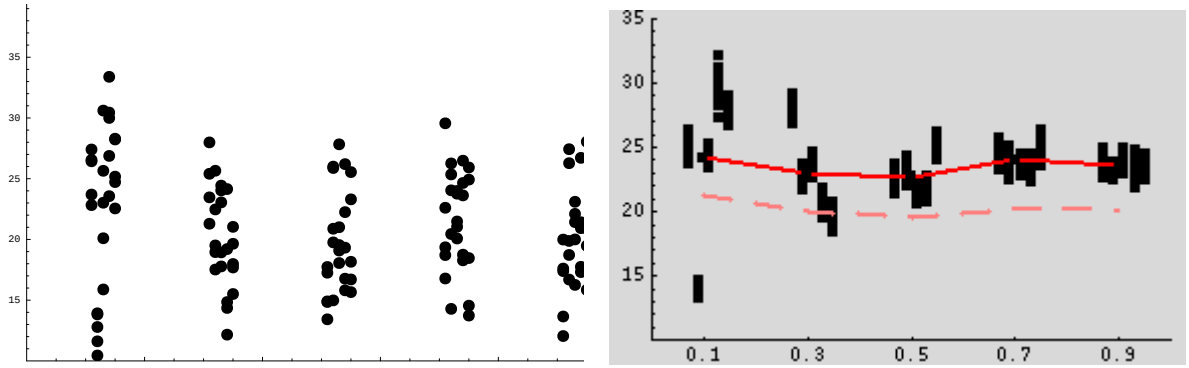

(a) (b)

FIGURE 4.6. Specificity of (a) the multiscale profile model and (b) the single-scale profile model, as a function of size of training population. Horizontal axis is as in Figure 4.4 (population sizes of 10%, 30%, 50%, 70%, and 90% of total). For each of 20 generated samples from each of 25 models the mean squared-difference in image intensity between the generated profile set and the closest profile set in the training population is plotted: lower is better. Solid line indicates mean specificity of the single-scale model for each size of training population; dashed line is for the multiscale model, for comparison.

As the size of the training population increases, the single-scale profile models show a convergence in MSD between randomly generated profile sets and the training populations. The multi-scale profile models show no such convergence, but the specificity is on average better than that obtained by the single-scale models, as seen by the solid (single-scale) and dashed (multiscale) lines in Figure 4.6(b). An interesting phenomenon

is that, for a fixed training population, randomly generated samples from the multiscale model lie within a wide range of distances from the training population, whereas randomly generated samples from the single-scale model are all about the same distance from the training population – the spread in specificity is tighter. One possible explanation could be that the multiscale model has increased flexibility to reproduce small-scale variability in the training population. The single-scale model may be consistent in the sort of profiles it generates, but it may be unable to capture the small-scale variability needed to come close to the individual training profiles.

Despite the difference in spread of specificity, my multi-scale model still shows significantly improved specificity over the single-scale profile model. Figure 4.3.1.2 shows the p-value of a one-sided T-test comparing the distribution of specificity from the multiscale model to the distribution from the single-scale model, using a pooled variance. This hypothesis test is done separately for each of the 25 choices of training population; no correction for multiple tests has been done.

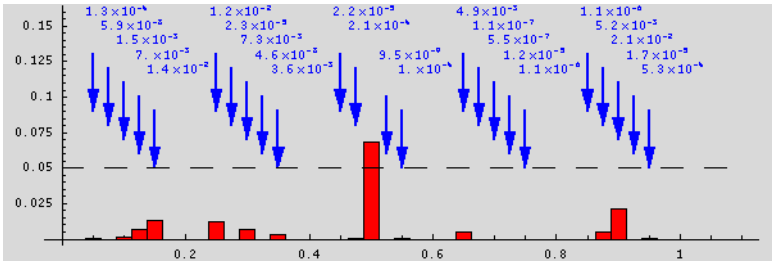

FIGURE 4.7. Improvement in specificity using multiscale model, p-values
p-values comparing specificity of the multiscale profile model with the single-scale profile model, derived from data in Figure 4.6. Columns highlighted with blue arrows are training populations that show a significant ($p < 0.05$) improvement in specificity in the multiscale profile model over the standard single-scale model.

4.3.1.3. *Variance.* Since both the new multiscale profile model and the standard single-scale profile model use Gaussians to represent local conditional probabilities, the variance of these local Gaussians serves as a measure of how "tight" the distribution is. For a unimodal distribution one would expect a high-specificity distribution to also exhibit tight variance. In the single-scale case there are 512 Gaussian distributions, one for

each profile on the boundary. In the multiscale case there are 512+128+32+8 Gaussian distributions, one for each location and scale according to the pyramidal sampling of scale space. For each local Gaussian the variance is taken as the trace of the covariance matrix (sum of eigenvalues). Figure 4.8(a) shows the sum of local variances for each of the 25 multiscale profile models. Instead of a sum of the local variances, a weighted sum could be used; however, the choice of weights is an open issue.

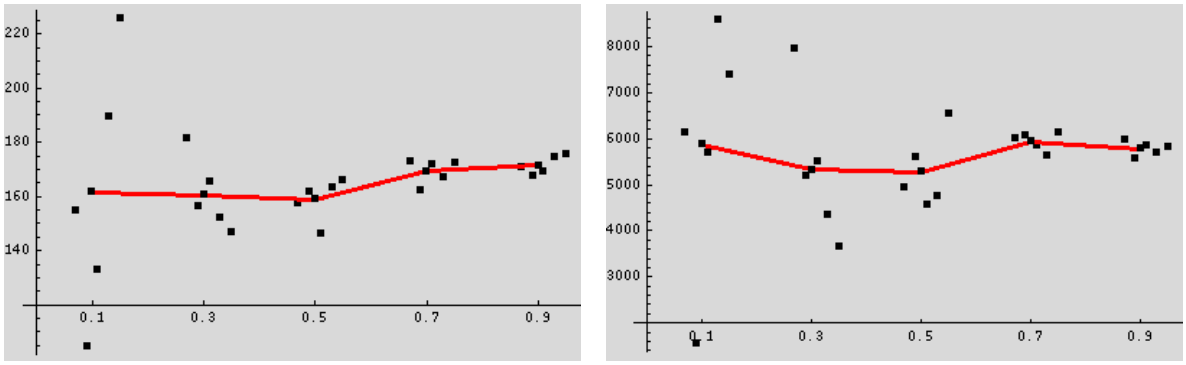

(a) (b)

FIGURE 4.8. Sum of local variance of (a) the multiscale profile model and (b) the single-scale profile model, as a function of size of training population. Axes are as in Figure 4.4.

Figure 4.8(b) shows the sum of local variances for each of the 25 single-scale profile models. The overall shape of convergence is similar to the multiscale models, with variance becoming more similar as training population size increases. This behavior is to be expected since all the training populations draw from the same pool of 114 subjects. However, note that the scale of the vertical axis in Figure 4.8(b) is twenty times that of Figure 4.8(a). The multiscale profile models have more local Gaussian models (512+128+32+8) than the single-scale models (512), and they have much lower variance, indicating that they model the population more tightly.

There are multiple sources of noise and variability in the images. The blurring in my multiscale profile model removes image noise which is independent of locality, thereby lowering variance. Variability across different patients is not, however, reduced by blurring in my multiscale model, since it only blurs within each image. My multiscale image

match model is motivated by a desire to capture the inter-patient variability in image appearance in a collar of interest about the boundary, while overcoming small-scale image noise.

Figure 4.9 takes a closer look at the variances of local Gaussian potentials for one particular training population (of size 70% of total). Figure 4.9(a) shows the variances of local potentials at the three finer scales of my multiscale profile model. The top level of scale is omitted in this graph since it is not a scale residual and hence is not commensurate with the features used in the finer scale levels. Figure 4.9(b) shows the variances of local potentials in the single-scale model. The ordering of points within each scale level is a consistent path across the 2D surface of the object. For comparison the dashed line in Figure 4.9(b) indicates the variance at the top level of the multiscale model; this is commensurate with the variances of the single-scale model shown in that graph.

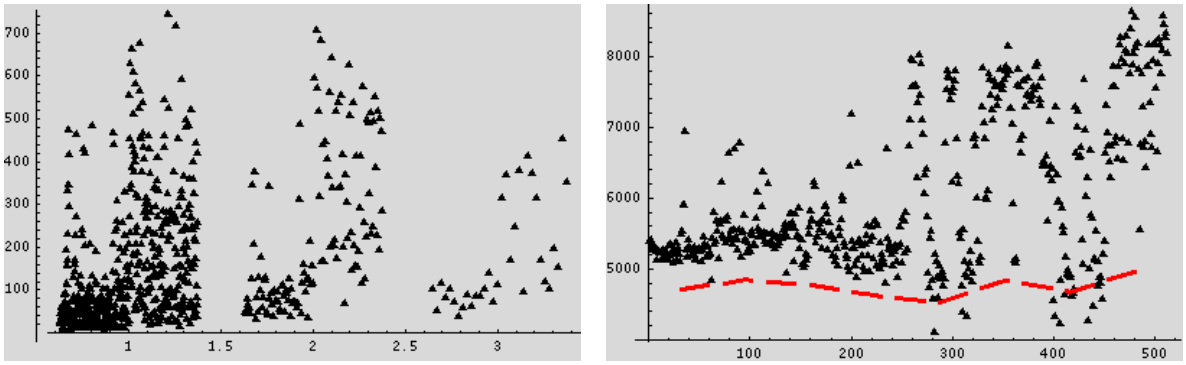

(a) (b)

FIGURE 4.9. Variance of local Gaussian potentials for a single training population. (a) Variance in the multi-scale model, separated by scale (fine, moderate, and coarse scale). (b) Variance in the single-scale model, sorted by locality. Dashed line indicates variance of top level of multiscale model, for comparison.

A dramatic tightening of variance is seen across all scales and localities in my multi-scale model. The Gaussian models at the top level of scale in the multiscale model are commensurate with the Gaussian models in the single-scale model, and the variances of the top level of scale in the multiscale model are uniformly tighter than the variances in the single-scale model.

Figure 4.10 shows another perspective on the variances of the Gaussian potentials used in the profile models. The *relative variance* of a Gaussian potential is the variance divided by the absolute value of the mean. For a multidimensional Gaussian I use the trace of the covariance matrix divided by the norm of the mean. The very small magnitude of the scale-residual features results in a large relative variance in my multiscale profile model at the finer scales. However, comparing the top level of my multiscale model to the single-scale profile model, relative variance is improved using my multiscale model. A possible interpretation is that my multiscale profile model isolates image noise in small-scale features with large relative variance, providing clean large-scale intensity features with comparatively small variance.

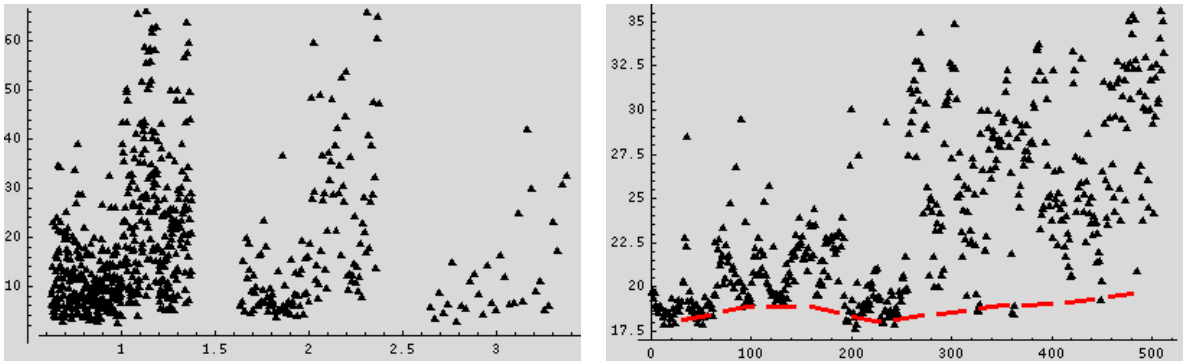

(a) (b)

FIGURE 4.10. Relative variance (variance divided by mean value) of local Gaussian potentials for a single training population. (a) Multi-scale model, separated by scale (fine, moderate, and coarse scale). (b) Single-scale model, sorted by locality. Dashed line indicates variance of top level of multiscale model, for comparison.

Certain localities on the boundary can be seen which show tighter variance than other localities, and this is consistent in both profile models. In this visualization, however, adjacent points on the graph do not necessarily correspond to adjacent localities on the object boundary. A 3D visualization is also useful.

In Figure 4.11 we see a visualization of the local variance texture-mapped onto the mean caudate shape in 3D, at different scales. Darker shades indicate smaller variance of the local profile model at that scale; lighter shades indicate larger variance. Since the top

level of scale does not model scale residuals (a la Laplacian pyramid) but blurred profiles (a la Gaussian pyramid), the variance is much larger than it is for the scale residuals. The variance of the scale residuals ranged from 7.7 to 1108; this is the range of the greyscale colormap visualization in Figure 4.11. The variance at the top level of scale averaged 4746; it was omitted from the figure in order not to skew the colormap. This figure is for one specific training population (the same as that used in Figure 4.9).

The visualization of local variance shows a patch midway near the tail of the caudate, of medium scale (Figure 4.11(b)), which has larger variance than other locations at other scales. The head of the caudate consistently abuts the lateral ventricle, but near the tail, the caudate separates from the ventricle. Variability in the location of separation from the ventricle results in variability in boundary profiles in that region; this may explain the increased local variance at that patch.

From Figure 4.11 a summary figure can be produced: for each patch on the boundary, an "optimal scale" for representation is selected, the scale at which the local variance is smallest. The top level of scale is not included in this optimal scale selection, since it is not commensurate with the other scales. Figure 4.12 shows the result, again texture-mapped onto the mean caudate shape.

Evaluated as a probabilistic model, my new multiscale profile model shows significantly improved specificity and tighter variance compared to the classical single-scale profile model. The validation study on generalizability shows that the two profile models do not differ significantly in generalizability. Trends can also be seen as the training population size is increased; both profile models improve with more training, particularly in variance. The specificity of the single-scale profile model improves with larger training populations, but the multiscale profile model consistently has signficantly better specificity at all sizes of training population.

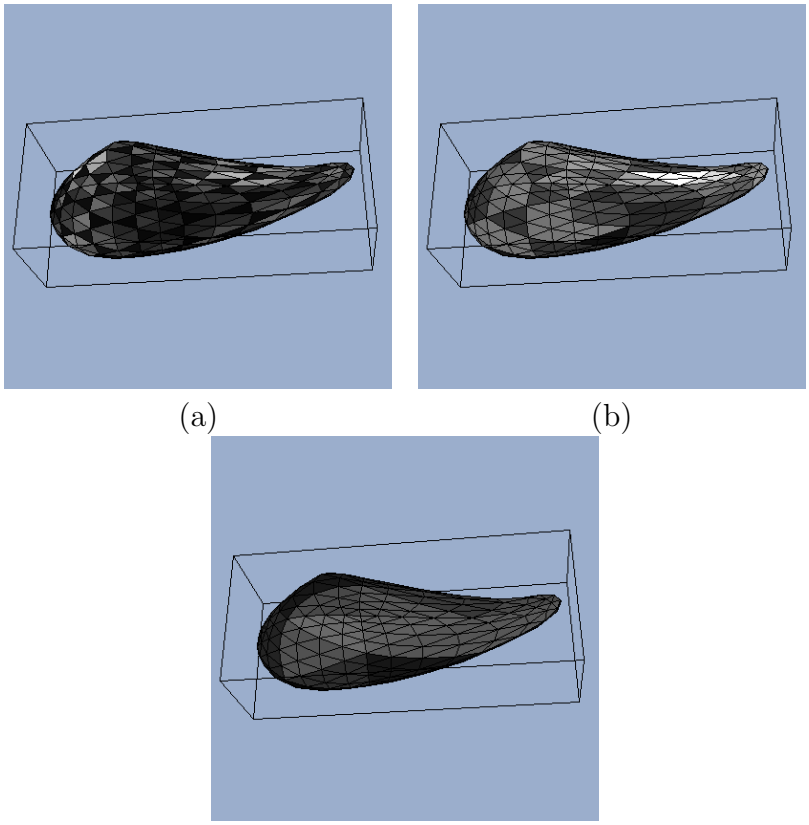

(a) (b)

(c)

FIGURE 4.11. Visualization of local variance in the multiscale profile model, with one training population. Dark indicates smaller variance; light larger variance (max 1108). Three scales are shown, from fine (a) to coarse (c). The colormap is the same for all three figures. A patch of medium scale near the tail of the caudate has high variance; the caudate separates from the ventricle near the tail, so the profiles are less consistent there.

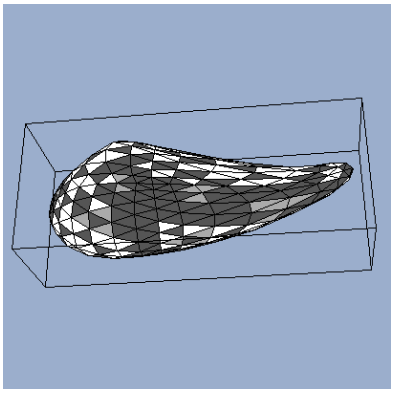

FIGURE 4.12. Automatic selection of optimal scale for each patch on the boundary: each patch is shaded according to the scale at which variance in the profile model (trace of covariance matrix) is smallest. Three scales are sampled from the scale space; darker is finer scale and brighter is coarser scale.

4.3.2. Evaluation in Segmentation. For each of the 25 divisions of the total population into test-vs-training subsets, five test images are randomly selected for segmentation. The implementation of the optimzation is as described in Section 4.1.4. Using the same shape prior, the segmentation is run once (until a threshold of convergence is met) with the new multiscale profile model and once with the standard single-scale profile model for comparison. The resulting segmentations are then compared with the expert manual segmentation of the test image.

Since the segmentations are run using the *SPHARM* shape representation, and I also have *SPHARM* representations of the manual segmentations, it is straightforward to calculate the mean squared-distance (MSD) between corresponding surface points. This uses a convenient property of the spherical harmonic orthonormal decomposition of shape, namely the Parseval equation:

$$\int_{S^2} |\mathbf{x}_1(\theta,\phi) - \mathbf{x}_2(\theta,\phi)|^2 \propto \sum_{l=0}^{\infty} \sum_{m=-l}^{l} ({c_1}_l^m - {c_2}_l^m)^2, \tag{79}$$

where $\mathbf{x}_1$ and $\mathbf{x}_2$ are the (x, y, z) coordinates of surface points on the two shapes to be compared and $\mathbf{c}_1, \mathbf{c}_2$ are the spherical harmonic coefficients of the respective shapes. Hence the mean squared-distance between corresponding surface points can be obtained directly from the *SPHARM* representations of the shapes. The MSD metric depends on the point-to-point correspondence defined by the *SPHARM* shape representation. Other shape difference metrics like volume overlap do not depend on correspondence, but they may have other issues instead.

Figure 4.13 shows the automatic segmentation results, formatted in the same way as the plots of model generalizability, variance, etc. The vertical axis indicates MSD in mm from the manual segmentation. Figure 4.13(a) uses my new multiscale profile model for image match; Figure 4.13(b) uses the classical single-scale profile model. The training populations, shape prior, model initialization, and optimization scheme are identical in both cases.

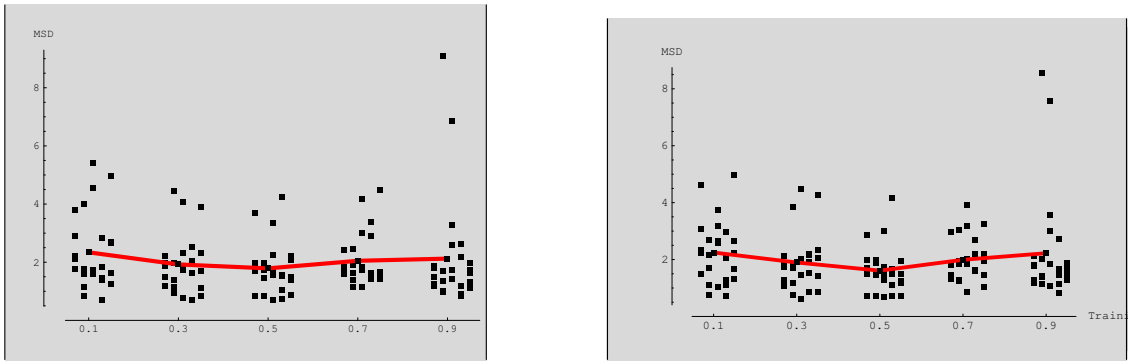

(a) (b)

FIGURE 4.13. Mean squared-distance between manual segmentation and automatic segmentation using (a) multiscale and (b) single-scale profile model. Horizontal axis is as in Figure 4.4, vertical axis is mm of distance.

The results do not show a significant change in segmentation accuracy by using my multiscale profile model instead of the classical single-scale profile model. Both automatic segmentation methods are in these tests largely unable to come closer than 2mm in MSD to the manual segmentations.

A major strength and motivation of scale-space representations is capturing moderate-scale and coarse-scale structures of interest while overcoming small-scale noise. In the high-resolution, high-quality, T1-weighted MRIs used in this study the signal-to-noise ratio is very good. One possible explanation for why my multiscale profile model does not show a significant improvement in segmentation is that the images are already "too clean", with insignificant small-scale noise. Figure 4.2 shows a slice through one of the images used in this study. Future validation studies could evaluate segmentation performance in the face of increasing amounts of artificially added image noise (e.g., Gaussian noise, independent at each voxel).

A complete automatic segmentation framework is much more than the image match model; the interaction between the image match model and the shape prior is important, as is the posterior optimization methodology. In my implementation I constructed the log-posterior as a weighted sum of the log-prior and log-likelihood, and I used Mathematica's conjugate-gradient optimizer as a "black-box" function to optimize the posterior.

However, poor control of the parameters of the optimizer may be biasing the results; the effect could be greater than any improvement in segmentation provided by my multiscale image match model.

Another factor in optimization is the parameter space over which optimization is performed. To ease the optimization I chose the optimization space to be an 18-dimensional space of 12 eigenloadings of shape deformation and 6 parameters for translation and rotation. Thus the range of shapes produced by the automatic segmentation is limited to the 12-dimensional subspace spanned by the 12 major modes of shape deformation. The manually segmented shape is not limited to this 12-dimensional subspace; hence the automatic methods might not be able to come close to the manual segmentation, regardless of which image match model is used. Future work to evaluate this hypothesis could use the full 504-dimensional *SPHARM* shape space as the optimization space (while keeping the same shape prior), or perhaps a final "lock-in" phase of segmentation where the shape is allowed freely to deform without being constrained to the 12-dimensional shape subspace.

The multiscale profile model also allows visualization of the image forces at work during the segmentation, at various levels of scale. Figure 4.14 shows a snapshot of one iteration of segmentation. The local image match (Mahalanobis distance) is shown for each patch of the boundary, at three levels of scale. The lighter shading at the tail of the caudate indicates worse fit; the visualizations also indicate that the fit is poor for a large-scale portion of the boundary rather than for a small patch of it.

The local segmentation error can also be texture-mapped onto the object surface in order to determine where the segmentation performed poorly and where it performed better. Figure 4.15 shows a visualization of segmentation error on a single case after many iterations of automatic segmentation using my multiscale image match model. The shading at each point indicates point-to-point distance between corresponding points on *SPHARM* representations of the automatic segmentation and a manual segmentation. Darker shades represent lower distance (better segmentation); lighter shades indicate

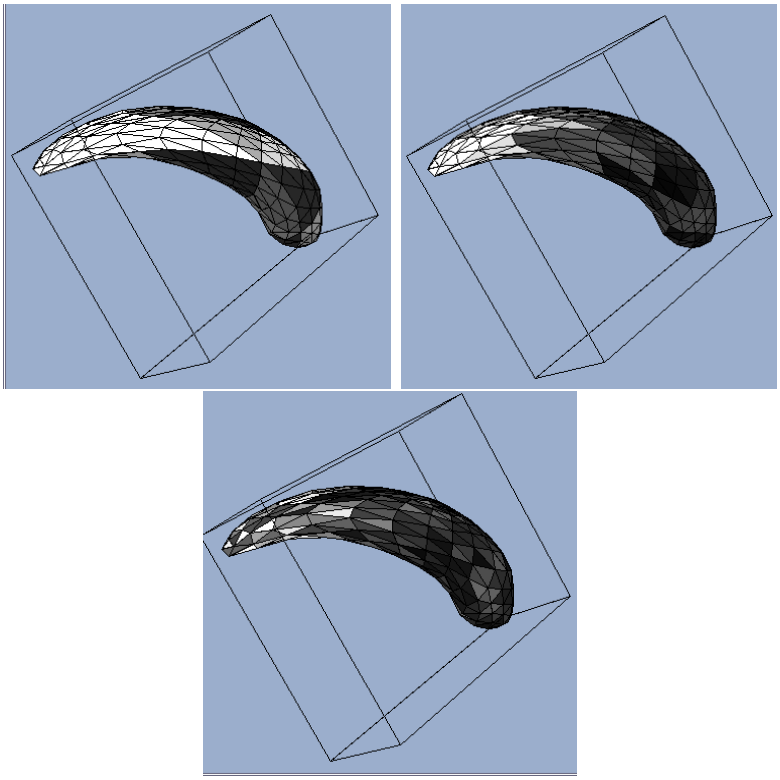

FIGURE 4.14. Visualization of local image match of the geometry to one target image during an early iteration of segmentation, at three levels of scale (coarse to fine). Light indicates worse fit, dark indicates better fit. The tail of the caudate has yet to fit into the image optimally at this iteration.

larger distance (worse error). Interestingly enough the segmentation error seems to be around the body of the caudate; the tail of the caudate is segmented to within 0.7mm of the manual rater gold standard. That the segmentation errors are not uniformly distributed over the surface indicates a systematic error; perhaps the automatic segmentation was not given enough iterations to reach convergence, or perhaps the shape space is excessively restrictive in allowable deformations.

4.3.2.1. *Manual Rater Reliability.* In this section I wish to evaluate the precision of the manual segmentations that were used as gold standards for my automatic segmentation schemes. I evaluate intra-rater and inter-rater reliability in manual segmentation for two human raters ("Rater A" and "Rater B") on a subset of images from the population. A similar study using a volume overlap measure is discussed in [Joshi et al. 2004]. In

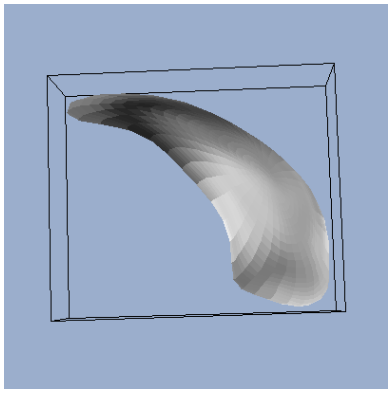

FIGURE 4.15. Visualization of local segmentation error after convergence. Darker shades indicate lower Euclidean distance to corresponding points on the gold standard; lighter shades indicate larger error. This segmentation used my multiscale image match model; results with the single-scale profile model are similar.

my study *SPHARM* boundary representations were obtained for each of the manual segmentations in the reliability study. Rather than volume overlap, the mean squared-distance (MSD) between corresponding boundary points is used as the metric to compare segmentations, to be consistent with the segmentation results presented in Figure 4.13.

Figure 4.16 shows average MSD for all pairs of segmentations for each of the five datasets, categorized into intra-rater and inter-rater figures. For example each point in the "Rater A" line represents three segmentations of each dataset; thus, there are three pairs of segmentations to consider, and the height of a point on that line indicates the average MSD across those three pairs. For the "A to B" column each dataset has three segmentations by rater A and three segmentations by rater B. There are nine pairings that compare A to B; the height of a point represents the average of those nine MSD of pairs.

We see that the manual raters achieve a very high degree of reliability, with on average about 0.4mm in MSD between repeated segmentations. The expert raters invested a number of months in developing a careful protocol for manual segmentation. In comparison neither of the automatic methods come within 2mm in MSD to the manual segmentation standard.

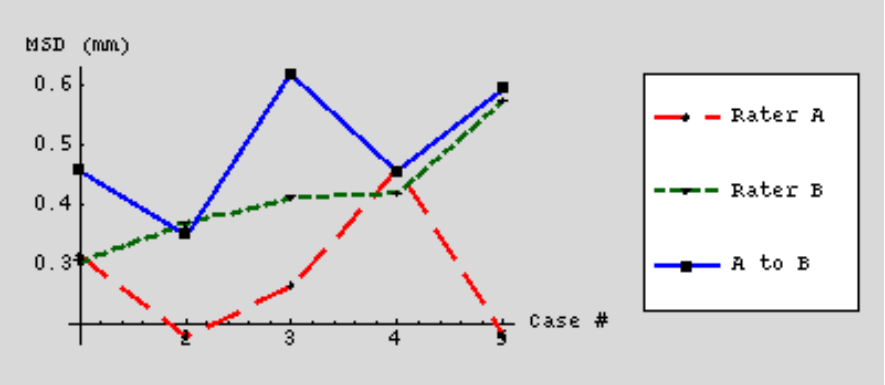

FIGURE 4.16. Intra-rater ("Rater A" and "Rater B") and inter-rater ("A to B") reliability for manual segmentation of five images, each repeated three times, by two expert raters ("Rater A" and "Rater B"). Reliability is measured by average MSD (mm) between all pairs.

4.3.3. Summary of Validation Results. I have compared my multiscale profile model for image match with a single-scale profile model similar to that used in Active Shape Models and Kelemen's *SPHARM* segmentation framework. My multiscale profile model has been validated both as a probabilistic model and as the image match component in deformable-models segmentation. As a probabilistic model, my multiscale profile model shows generalizability that is comparable to that of the single-scale profile model, but my model exhibits significantly improved specificity and tighter variance as compared to the single-scale profile model. In segmentation tests automatic segmentations using both my model and the single-scale model were compared with manual segmentations by human raters. Accuracy of segmentation was evaluated by mean squared distance to the manual segmentation. Automatic segmentations using my multiscale image match model did not show significantly improved accuracy over automatic segmentations using the single-scale image match model.

These results show that although my multiscale profile model is a significant improvement over the single-scale profile model in specificity and variance, more validation tests are needed before I can claim that segmentation quality is improved by using my multiscale image match model. As a statistical model my multiscale model more precisely models training populations than the classical single-scale profile model does. My profile

model can find immediate application in population understanding; it can provide insight at multiple scales into the structure and variability of image appearance in a collar of interest about the object boundary. The segmentation tests in this study do not show an improvement in segmentation accuracy by using my multiscale image match model instead of the classical single-scale profile model. However, future tests using more noisy images may show that my multiscale image match model is more robust to increasing image noise.

CHAPTER 5

Conclusion

5.1. Summary

This dissertation explored multiscale image match for Bayesian segmentation. The new profile model I presented is statistical, multiscale, and uses object-intrinsic coordinates: it is statistically trained on a population of segmented images, it uses a scale space on profiles, and the scale space performs blurring in the parameter space of the *SPHARM* shape representation. The profile scale space distinguishes between along-boundary and across-boundary directions, enabling a model that follows Canny's concept of blurring along the boundary but performing edge localization across the boundary. The current implementation does not perform any blurring or derivatives in the across-boundary direction, but such extensions would be natural for future work.

My multiscale profile model as described in Chapter 3 uses a novel scale space on scalar-valued functions defined on a manifold $\mathcal{M}$, representing the 2D surface of the object in 3D. I solve the heat equation on $\mathcal{M}$ by using a diffeomorphic map from the sphere S^2, provided by the *SPHARM* shape representation. The solution to the heat equation on the sphere is available in closed-form by using a spherical harmonic orthonormal basis representation of the scalar-valued function. Thus, in my implementation the use of spherical harmonics as an orthonormal basis for shape representation is parallelled by the use of spherical harmonics as an orthonormal basis for representation of the image intensities about the object boundary.

A probability distribution is put on the profile scale space by sampling a pyramid in scale; the resulting tree of multiscale profiles is modelled with a Markov Random Field using local Gaussian potentials. This produces a probabilistic model on image intensities

in a collar about the object boundary that is statistically trained and multiscale, using object-intrinsic coordinates to parameterize the profiles. This probabilistic model can then be used as an image match model in a Bayesian segmentation framework.

In Chapter 4 I validated my multiscale profile model as implemented in my Mathematica testbed software framework. To evaluate its efficacy as a probabilistic model, I examined its generalizability, specificity, and variance on multiple training populations of various sizes. For comparison I implemented a single-scale profile model similar to that used in Active Shape Models and Kelemen's *SPHARM* segmentation framework. Jackknife tests were run on 25 randomly chosen training populations, of sizes ranging from 10% to 90% of a total pool of 114 segmented images. The validation tested whether my multiscale profile model modelled the training populations better than the classical single-scale profile model, and it also examined the behavior of the profile models as training size increases. The results showed that my multiscale profile model exhibits significantly improved specificity and tighter variance as compared to the single-scale profile model; the generalizability is comparable.

I also implemented a full segmentation framework with an option to toggle between my multiscale image match model and the classical single-scale image match model. 125 test segmentations were run using each image match model, and the results were compared to expert manual segmentations. This validation tested whether my multiscale image match model improved segmentation accuracy over the classical single-scale profile model. In these tests no significant improvement in segmentation accuracy was shown, but future work remains to be done on evaluating the efficacy of multiscale profile models in a full segmentation framework.

5.2. Discussion

Is a multiscale image match model worth the added complexity over the well-known single-scale profile model? I believe the validation results show that my multiscale profile model is a significant improvement over the classical single-scale profile model for the purpose of population modelling and analysis. The significant improvements in specificity and variance indicate that my new multiscale model has more flexibility to model structure and variability in profiles at multiple scales. This could have immediate application in understanding expected image appearance in a collar of interest about the object boundary, as well as understanding where about the object one would expect larger variability in image intensity. There are potential applications in pathology discrimination, as well: there are clinical hypotheses that some pathologies may be correlated with change within tissue resulting in change in MR image intensity rather than shape change. For such applications my multiscale profile model would be useful for capturing that change in MR intensity at scale while overcoming image noise. These are all applications that use my multiscale profile model as a statistical model by itself, outside of a segmentation framework.

My new multiscale profile model also shows promise for use as an image match model in a full segmentation framework. The results I presented of the segmentation tests are perhaps a bit disappointing in that no significant improvement in segmentation accuracy relative to manual segmentations is shown; for segmentation on these datasets one might as well use the old single-scale profile model. However, as mentioned in Section 4.3.2, there are a number of potential future validation studies that could be run to explore further the performance of my multiscale image match model in segmentation.

Since scale space is traditionally often used to capture medium-scale and large-scale structures in the face of small-scale noise, future work might evaluate segmentation of images with increasing amounts of artificially added image noise. The test images used in my validation study have very high signal-to-noise ratios, but not all images are so

"clean", and a multiscale image match model that is robust to image noise would significantly improve segmentation of noisy images. Another possible factor contributing to the poor segmentation results is the restriction of allowable deformations to the 12-dimensional shape PCA space, rather than the full 504-dimensional space of possible shapes. This severe restriction may prevent the automatic segmentation from coming close to the manual result, regardless of which image match model is used. In my segmentation tests, I also felt that details of the posterior optimization technique strongly influenced the automatic segmentations; it is possible that the segmentation converged slowly enough that it did not converge in the allowed number of iterations, or that the segmentation converged to a local extremum. The current implementation of scale space in my method depends on correspondence given by the equal-area *SPHARM* parameterization; future work could implement a discrete Laplace-Beltrami blurring directly on the surface of the object, thus gaining independence from the correspondence imposed by the shape representation.

I believe that a multiscale image match model is a worthwhile pursuit and that my particular multiscale profile model has demonstrated significant improvement over the classical single-scale profile model, for the purpose of population modelling and analysis. For use in segmentation my multiscale image match model shows promise, and I believe future work will show more clearly the situation under which my multiscale model significantly improves segmentation.

5.3. Contributions to Knowledge

This dissertation has made a number of novel contributions to the body of knowledge in image match modelling; these are outlined in this section.

The complex image appearance of anatomical structures in noisy medical images motivates a multiscale approach to statistical modeling of image profiles. Traditional profile models represent the profiles at a scale determined by the image acquisition process (e.g., MRI scanner resolution) and do not take advantage of the expected high degree of similarity between adjacent profiles. Traditional multiscale approaches perform blurring in Euclidean image space, resulting in blurring across object boundaries, potentially destroying important boundary profile information. My new profile scale space makes use of the *SPHARM* shape representation to map the boundary profiles onto the sphere S^2, where a scale space is defined that blurs image intensities along the object boundary, but not across the boundary.

The definition of scale space on a domain of S^2 is a novel contribution that to my knowledge has not previously been done in this context. The use of the S^2 scale space and the *SPHARM* shape representation to define a scale space on an arbitrary manifold diffeomorphic to the sphere is also a novel contribution of this work. This is a scale space in object-intrinsic coordinates. Finally, the construction of a Markov Random Field model on features sampled from the profile scale space is also a new contribution to the theory.

I have validated my new multiscale profile model by comparing it to the classical single-scale profile model used in Active Shape Models and Kelemen's *SPHARM* segmentation framework. The quality of the model has been evaluated in the areas of generalizability, specificity, and variance. The two profile models show comparable generalizability, but my multiscale profile model exhibits significantly improved specificity and tighter variance. The performance of the two profile models in segmentation has also been evaluated. Although the experiments run do not show significant improvement in segmentation accuracy using my new multiscale image match model, further experiments

are proposed to highlight situations where a multiscale image match may show significant improvement in segmentation accuracy.

5.4. Future Work

The results I have shown in this dissertation are exploratory analyses, showing encouraging results suggesting that multiscale profile models are a worthwhile avenue of research. There are many possible future directions of research; this section discusses a few possible ideas.

5.4.1. Comparison with Laplace-Beltrami Smoothing. The main thesis of this dissertation is that multiscale profile models are an improvement over the classical single-scale profile model. However, there are many ways to define a multiscale profile model; only one is examined in this dissertation. For instance there are other possible scale spaces for scalar functions on the object boundary manifold $\mathcal{M}$. Section 3.1.4 discusses the scale space I use on the boundary manifold $\mathcal{M}$ in comparison with a Laplace-Beltrami solution of the heat equation on the manifold. A validation study comparing blurring by my method using the *SPHARM* diffeomorphic map with blurring by Laplace-Beltrami smoothing would be useful. Section 3.1.4 outlines one possible implementation of a first-order approximation to Laplace-Beltrami blurring on the manifold $\mathcal{M}$.

If the results of blurring via these two methods are similar, the choice of which one to use can be made on the basis of ease of implementation and computational efficiency. If the scale spaces are not similar, the study may be a useful illustration of how the correspondence from the geometric model influences my scale space as compared to the "coordinate-free" Laplace-Beltrami smoothing.

5.4.2. Features in the Across-Boundary Direction. In this dissertation the emphasis has been on multiscale profile models where the scale is in the along-boundary directions; in the across-boundary direction each profile has been seen as a vector of unnormalized image intensities. Future work could use multiscale profile features where the scale in the across-boundary direction is independent of the scale in the along-boundary direction. Instead of unnormalized image intensities, a derivative or n-jet of image intensities could be used in the across-boundary direction. The single-scale profile model

to which I compare my multiscale model is in fact not the same as the profile model used in Active Shape Models; ASMs use derivatives along the profile instead of unnormalized image intensities. Instead of a vector of image intensities, each profile could also be represented by a set of coefficients of Legendre polynomials or some other orthogonal transform (discussions with Florack et al.).

5.4.3. Multi-Grid Optimization. The work in this dissertation develops a multiscale representation and statistical model for image appearance in a collar about the object boundary. Others have worked on object shape representations that are multiscale, allowing deformation and analysis of geometry at multiple scales. It may be desirable to combine multiscale shape with multiscale profiles. During segmentation coarse-scale deformations of the geometry could be done first, using coarse-level profiles for the image match. As the optimization progresses, the geometry moves to finer-scale deformations, using profiles at a correspondingly finer scale.

The *SPHARM* shape representation uses a frequency decomposition of shape, but frequency in spherical harmonics is not the same as the scale in my profile scale space. The *SPHARM* frequency decomposition provides levels of detail, but the scale in my profile scale space is an aperture of measurement. Perhaps the shape deformations could be smoothed in the same way that the profiles are smoothed, using a $e^{-l(l+1)2\sigma^2}$ modulation of spherical harmonic coefficients. M-reps [Pizer et al. 1999] represent shape in a very different way, with another concept for multiscale shape representation. It would be worthwhile to compare the m-reps concept of aperture scale with my definition of scale for profiles, to build a synchronized multiscale object representation in which the scale of image representation is linked with the scale of shape representation.

5.4.4. Extension to M-reps. I present a scale space on profiles that utilizes the *SPHARM* shape representation for the geometry of the object; this provides a diffeomorphic map from the object boundary to the sphere S^2, which is a simpler parameter space. A similar approach could be taken to apply my profile scale-space concept to the m-rep shape representation [Joshi et al. 2002] The object-intrinsic coordinate system of

m-reps provides a parameterization of the object boundary – indeed, of a whole volume of interest encompassing the whole of the interior of the object and a collar of some thickness outside the object. The parameter space of this coordinate system is simply a rectangle in 2D (parameterizing the object boundary) or 3D (parameterizing the volume of interest). The rectangular parameter space in 2D has wraparound at the edges so that it is topologically equivalent to a sphere. For more details on this parameterization see [Pizer et al. 2003]. The mapping to a parameter space encompasses the definition of correspondence and metric tensor on the volume of interest; this metric tensor is not the same as the one obtained by embedding the object in Euclidean space.

Once the image in the volume of interest has been mapped to the parameter space, a rectangle in 3D (with wraparound), a scale space on that profile image can be built in the usual fashion, similarly to how linear scale-spaces are built in Euclidean space. The across-boundary and along-boundary directions are logically separated in the parameter space. The wraparound effects are equivalent to boundary conditions on the solution of the heat equation. In fact, standard Fourier-space implementations of linear scale space on a bounded domain in Euclidean space often assume boundary conditions that are equivalent to cyclic wraparound [Romeny 2003].

This would allow an object-intrinsic scale space to be defined on the image in a volume of interest about an m-rep-defined object, taking advantage of the parameterization (and hence definition of correspondence) given by the m-rep shape representation. The m-rep parameterization of the collar about the boundary avoids some problems, mentioned in the next section, which are present in the straight-line profiles I used in my present implementation. Such an object-intrinsic image scale space could then be sampled in a pyramidal fashion, and the scale residuals could be used as features in a multiscale image match model for m-rep segmentation.

5.4.5. Extension to Flow-Field Profiles. The implementation presented uses the *SPHARM* shape representation based on spherical harmonics, but the idea of a scale space on image profiles about an object is generalizable to other shape representations. A

key element is how profiles are defined from the object geometry. If a multiscale statistical image match model similar to ours is to be used with a different shape representation, the geometric representation needs to provide a parameterization of the region of interest Ω from which the profiles are sampled. In order to preserve the "across-boundary" vs. "along-boundary" distinction a la Canny, the parameterization needs to provide a local frame at each point in Ω that distinguishes across-boundary directions from along-boundary directions.

In this section a generalization to the *SPHARM*-based profile scale space is presented, using a more general shape representation inspired by theory from [Damon 2003a,b, 2004]. The parameterization of profiles in the region of interest Ω is denoted by a flow-field U from a base manifold $\mathcal{M}$. This provides a general framework that can be applied to various shape representations, including *SPHARM*, Point Distribution Models (PDM), and m-reps. This section also discusses instantiation of the general framework to the *SPHARM* and m-rep shape representations.

Let $\mathcal{M}$ be the *skeletal manifold*, the manifold from which profiles flow. In this section $\mathcal{M}$ no longer needs to be diffeomorphic to a sphere; for instance, it could have a boundary. Let $\mathcal{M}$ be parameterized by $\mathbf{u}$. In the case of the *SPHARM* representation, $\mathcal{M}$ is simply the object boundary; $\mathbf{u} = (\theta, \phi) \in S^2$. In the m-rep case, $\mathcal{M}$ is the medial manifold, parameterized by $\mathbf{u} = (u, v)$.

Let $U : \mathcal{M} \times [0, 1] \rightarrow \Omega$ by $(\mathbf{u}, \tau) \mapsto \mathbf{x}$ be a flow-field from $\mathcal{M}$ that is one-to-one and onto, although possibly multivalued. This defines the shape of the profiles; in the case of my *SPHARM*-based implementation, U flows along straight lines normal to the boundary. In the m-rep case, U flows along radial lines from the medial manifold out to the medial approximation to the object boundary; it flows along curved lines a short distance beyond the boundary, up to caustics outside the object. Ω is the collar of interest about the boundary. One-to-one in this multivalued context means that if any value of $U(\mathbf{u}, \tau)$ coincides with any value of $U(\mathbf{u}', \tau')$, then $\mathbf{u} = \mathbf{u}'$ and $\tau = \tau'$. Also, for every

"onionskin" level τ, assume that $U(\tau) = \{U(\mathbf{u}, \tau) : \mathbf{u} \in \mathcal{M}\}$ is a differentiable manifold (possibly a manifold with boundary).

Let $f \in L^2(\Omega)$ be a scalar function defined on the region of interest. In this application f is simply the image, in the region of interest.

For every τ, if the "onionskin" $U(\tau)$ is a Riemannian manifold, it has a Laplace-Beltrami operator, call it $\triangle_\tau$. Let the function $f_\tau : U(\tau) \to \mathbb{R}$ be the restriction of f to the manifold $U(\tau)$. Since $f \in L^2(\Omega), f_\tau \in L^2(U(\tau))$. Define the *tangential scale space* of f_τ to be the function $\Phi_T^\tau(f_\tau) : U(\tau) \times \mathbb{R}^+ \to \mathbb{R}$ that satisfies the heat equation

$$\frac{\partial \Phi_T^\tau(f_\tau)}{\partial \sigma_\tau} = \triangle_\tau \Phi_T^\tau(f_\tau)$$

subject to the boundary condition of convergence to f_τ at zero scale:

$$\lim_{\sigma_T \to 0^+} \Phi_T^\tau(f_\tau)(\cdot, \sigma_T) = f_\tau(\cdot)$$

To handle all "onionskin" levels τ at once I define the *tangential scale-space operator* $\Phi_T : L^2(\Omega) \to L^2(\Omega \times \mathbb{R}^+)$ as

$$\Phi_T(f)(\mathbf{x}, \sigma_T) = \Phi_T^\tau(f_\tau)(\mathbf{u}_\tau, \sigma_T),$$

where $\mathbf{u}_\tau \in U(\tau)$. τ is obtained through the inverse mapping $U^{-1} : \Omega \to \mathcal{M} \times [0, 1]$.

In the radial direction, let $\triangle_R$ be the Laplace-Beltrami operator on the interval $[0, 1]$, operating on each profile separately. Let the *radial scale-space operator* $\Phi_R : L^2(\Omega) \to L^2(\Omega \times \mathbb{R}^+)$ be the solution of the differential heat equation on $[0, 1]$:

$$\frac{\partial \Phi_R(f)}{\partial \sigma_R} = \triangle_R \Phi_R(f)$$

subject to the boundary condition

$$\lim_{\sigma_R \to 0^+} \Phi_R(f)(\mathbf{x}, \sigma_R) = f(\mathbf{x}).$$

Finally, the combined *scale-space operator* is $\Phi : L^2(\Omega) \to L^2(\Omega \times \mathbb{R}^+ \times \mathbb{R}^+)$ defined as

$$\Phi(f)(\mathbf{x}, \sigma_T, \sigma_R) = \Phi_T(\Phi_R(f)(\cdot, \sigma_R), \sigma_T),$$

where $\Phi_R(f)(\cdot, \sigma_R)$ represents the function in $L^2(\Omega)$ satisfying $\Phi_R(f)(\cdot, \sigma_R)(\mathbf{x}) = \Phi_R(f)(\mathbf{x}, \sigma_R)$.

This constructs a scale space on the collar of interest Ω, where the scales in the tangential and radial directions can be controlled independently. The flow-field representation is general enough to include both m-rep profiles and *SPHARM*-based straight-line profiles as special cases. Correspondence between instances of an object is provided by a parameterization of the collar of interest, which is encoded in the skeletal manifold and flow field.

5.4.6. Local Confidence Rating of Image Match. At each step of Bayesian segmentation there is one number that represents the shape typicality at that iteration and one number that represents the geometry-to-image match at that iteration. However, at some locations we may know in advance that the image match is not "trustworthy"; perhaps there is larger variability in image intensities about that point. This could be because of poor point-to-point correspondence, or the images may truly have larger variability there. In either case it may be useful to have a local confidence rating of the image match, in order to deweight the influence of the image match and defer to the shape prior at that location. If the image match at a point on the boundary is not trustworthy, then regardless of whether there is a good match or a poor match the influence of the likelihood should be deweighted at that point.

My image match model provides one possible source for a local confidence rating of image match; this is the variance of local Gaussian potentials (see Section 4.3.1.3). Where the variance is large, the profiles show large variability and might not be trustworthy; hence, the posterior should emphasize the shape prior more. Where the variance is small, the profiles are consistent, so the posterior can trust the output of the image match. Other sources for the local confidence rating could also be considered.

5.4.7. Image Match Model Quality as a Measure of Correspondence. Point-to-point correspondence, or homology, is a challenging issue that in this dissertation I have largely side-stepped. My implementation uses the default equal-area correspondence given by the *SPHARM* shape representation, but could be adapted to use any other parameterization of the object boundary. Many others have worked on the issue of correspondence; each producing a new metric for what defines "good" correspondence for a particular purpose.

Just as the variance of local Gaussian potentials in my multiscale profile model could be used as a local confidence rating in the image match, it could also be used as a rating of quality of point-to-point correspondence on a population of objects. If the correspondence among a population of objects is good, it is expected that variability in the profiles would be reduced.

5.5. Conclusion

In this dissertation I proposed a novel multiscale statistical model of image appearance in a collar of interest around an object boundary, suitable for use as image match likelihood in a Bayesian segmentation framework. My multiscale profile model uses a novel scale space on scalar-valued functions defined on a manifold $\mathcal{M}$, representing the 2D surface of the object in 3D. My probabilistic model has been validated on a large population of segmented images, and shows significantly improved specificity and variance as compared to the classical single-scale profile model. I have also run segmentation tests in a self-contained full segmentation framework incorporating my multiscale image match model. This image match model shows promise for use in segmentation of noisy images, and it is immediately applicable to problems of population analysis and discrimination, for understanding of image appearance in a region of interest about an object boundary.

BIBLIOGRAPHY

J. Blom. *Affine Invariant Corner Detection*. PhD thesis, Utrecht University, 1991.

C. Bouman and M. Shapiro. A multiscale random field model for bayesian image segmentation. *IEEE Transactions on Image Processing (TIP)*, 3(2):162–177, March 1994.

Peter J. Burt and Edward H. Adelson. The Laplacian Pyramid as a compact image code. *IEEE Transactions on Communications*, COM-31,4:532–540, 1983.

G. Gerig C. Brechbühler and O. Kubler. Parameterization of closed surfaces for 3-d shape description. *Computer Vision and Image Understanding (CVIU)*, 61:154–170, 1995.

J.F. Canny. A computational approach to edge detection. *IEEE Transactions on Pattern Analysis and Machine Intelligence (PAMI)*, 8(6):679–697, November 1986.

V. Caselles, R. Kimmel, and G. Sapiro. Geodesic active contours. *International Journal of Computer Vision (IJCV)*, pages 61–79, 1997.

H. Choi and R. Baraniuk. Multiscale image segmentation using wavelet-domain hidden markov models. *IEEE Transactions on Image Processing (TIP)*, 10(9):1309–1321, September 2001.

M.K. Chung, K.J. Worsley, J. Taylor, J.O. Ramsay, S. Robbins, and A.C. Evans. Diffusion smoothing on the cortical surface. *NeuroImage*, 13S(95), 2001.

T. Cootes, C. Taylor, and A. Lanitis. Active shape models: Evaluation of a multiresolution method for improving image search, 1994.

Timothy F. Cootes, Gareth J. Edwards, and Christopher J. Taylor. Active appearance models. *IEEE Transactions on Pattern Analysis and Machine Intelligence (PAMI)*, 23(6):681–685, 2001.

Timothy F. Cootes, A. Hill, Christopher J. Taylor, and J. Haslam. The use of active shape models for locating structures in medical images. In *Information Processing in Medical Imaging (IPMI)*, pages 33–47, 1993.

James Damon. Smoothness and geometry of boundaries associated to skeletal structures I: Sufficient conditions for smoothness. *Annales de Institut Fourier*, 53(6):1941–1985, 2003a.

James Damon. Smoothness and geometry of boundaries associated to skeletal structures II: Geometry in the Blum case. *To appear, Composition Mathematica*, 2003b.

James Damon. Determining the geometry of boundaries of objects from medial data. *To appear, International Journal of Computer Vision*, 2004.

Rh. H. Davies, C.J. Twining, T.F. Cootes, P.D. Allen, and C.J. Taylor. Shape discrimination in the hippocampus using an MDL model. In *Information Processing in Medical Imaging (IPMI)*, volume 2732 of *Lecture Notes in Computer Science*, pages 38–50. Springer, 2003. ISBN 3-540-40560-7.

Rhodri Davies. *Learning Shape: Optimal Models for Analysing Shape Variability*. PhD thesis, University of Manchester, Manchester, United Kingdom, 2002.

Mathieu Desbrun, Mark Meyer, Peter Schröder, and Alan H. Barr. Implicit fairing of irregular meshes using diffusion and curvature flow. *Computer Graphics*, 33:317–324, 1999.

A. Doucet. On sequential monte carlo sampling methods for bayesian filtering. Technical Report CUED/F-INFENG/TR. 310, Cambridge University Department of Engineering, 1998.

R. Duits, L.M.J. Florack, J. de Graaf, and B.M. ter Haar Romeny. On the axioms of scale-space theory. *Journal of Imaging and Vision*, 20(3):267–298, 2004.

Nicolae Duta, Anil K. Jain, and Marie-Pierre Dubuisson-Jolly. Learning-based object detection in cardiac MR images. In *International Conference on Computer Vision (ICCV)*, pages 1210–1216, 1999.

Samuel D. Fenster and John R. Kender. Sectored snakes: Evaluating learned-energy segmentations. *IEEE Transactions on Pattern Analysis and Machine Intelligence*, 23(9):1028–1034, 2001.

L. M. J. Florack, B. M. ter Haar Romeny, J. J. Koenderink, and M. A. Viergever. The Gaussian scale-space paradigm and the multiscale local jet. *International Journal of Computer Vision (IJCV)*, 18(1):61–75, April 1996.

L.M.J. Florack, B.M. ter Haar Romeny, J.J. Koenderink, and M.A. Viergever. Scale and the differential structure of images. *Image and Vision Computing*, 10(6):376–388, 1992.

S. Geman and D. Geman. Stochastic relaxation, gibbs distributions and the bayesian restoration of images. *IEEE Transactions on Pattern Analysis and Machine Intelligence (PAMI)*, 6(6):721–741, 1984.

J. M. Hammersley and P. E. Clifford. Markov fields on finite graphs and lattices, 1972. unpublished manuscript.

Chris Harris and Mike Stephens. A combined corner and edge detector. In M. M. Matthews, editor, *Proceedings of the 4th ALVEY vision conference*, pages 147–151, University of Manchester, England, September 1988.

S. Joshi, S. Pizer, P.T. Fletcher, P. Yushkevich, A. Thall, and J.S. Marron. Multi-scale deformable model segmentation and statistical shape analysis using medial descriptions. *IEEE Transactions on Medical Imaging (TMI)*, 21(5):538–550, May 2002.

S Joshi, S Pizer, T Fletcher, A Thall, and G Tracton. Multi-scale 3-D deformable model segmentation based on medial description. In MF Insana and RM Leahy, editors, *Information Processing in Medical Imaging (IPMI)*, volume 2082, pages 64–77, June 2001.

Sarang Joshi, Brad Davis, Matthieu Jomier, and Guido Gerig. Unbiased diffeomorphic atlas construction for computational anatomy. *To appear in NeuroImage*, August 2004.

M. Kass, A. Witkin, and D. Terzopoulos. Snakes: Active contour models. In *Proc. of IEEE Conference on Computer Vision*, pages 259–268, London, England, 8-11 1987a.

M. Kass, A. Witkin, and D. Terzopoulos. Snakes: Active shape models. *International Journal of Computer Vision*, 1:321–331, 1987b.

András Kelemen, Gábor Székely, and Guido Gerig. Elastic model-based segmentation of 3d neuroradiological data sets. *IEEE Transactions on Medical Imaging (TMI)*, 18: 828–839, October 1999.

J. J. Koenderink. The structure of images. *Biological Cybernetics*, 50:363–370, 1984.

Arjan Kuijper. Axioms, December 2003. presentation in PhD course on scale-space: `http://www.itu.dk/people/arjan/course/arjan/axiomatics/axioms.ppt`.

M. Leventon, O. Faugeraus, and W. Grimson. Level set based segmentation with intensity and curvature priors. In *Workshop on Mathematical Methods in Biomedical Image Analysis Proceedings (MMBIA)*, pages 4–11, June 2000.

Tony Lindeberg. *Scale-space Theory in Computer Vision*. Kluwer Academic Publishers, Stockholm, Sweden, 1994. ISBN 0-7923-9418-6.

Jun Liu, Lei Wang, and Stan Z. Li. MRMRF texture classification and MCMC parameter estimation, 1999.

R. Malladi, J.A. Sethian, and B.C. Vemuri. Shape modeling with front propagation: A level set approach. *IEEE Transactions on Pattern Analysis and Machine Intelligence*

(PAMI), 17(2):158–175, 1995.

M. I. Miller, S. C. Joshi, and G. E. Christensen. *Large Deformation Fluid Diffeomorphisms For Landmark and Image Matching*, pages 115–131. Academic Press, 1999.

Claus Müller. *Spherical Harmonics*. Number 17 in Lecture Notes in Mathematics. Springer-Verlag, 1966.

P. Perona and J. Malik. Scale-space and edge detection using anisotropic diffusion. *IEEE Transactions on Pattern Analysis and Machine Intelligence (PAMI)*, 12(7):629–639, July 1990.

S. Pizer, D. Fritsch, P. Yushkevich, V. Johnson, and E. Chaney. Segmentation, registration, and measurement of shape variation via image object shape. *IEEE Transactions on Medical Imaging (TMI)*, 18:851–865, October 1999.

SM Pizer, T Fletcher, A Thall, M Styner, G Gerig, and S Joshi. Object models in multiscale intrinsic coordinates via m-reps. *Image and Vision Computing*, 21(1): 5–15, January 2003. Special issue on Generative-Model-Based Vision (GMBV2002).

Bart M. Ter Haar Romeny. *Front-End Vision & Multi-Scale Image Analysis: Multi-Scale Computer Vision Theory & Applications*. Kluwer Academic Publishers, October 2003.

Peter Schröder and Wim Sweldens. Spherical wavelets: efficiently representing functions on the sphere. *Computer Graphics*, 29(Annual Conference Series):161–172, 1995.

I.M. Scott, Tim Cootes, and Chris Taylor. Improving appearance model matching using local image structure. In *Lecture Notes in Computer Science (LNCS): Information Processing in Medical Imaging (IPMI)*, volume 2732, pages 258–269. Springer-Verlag, 2003.

L.H. Staib and J.S. Duncan. Boundary finding with parametrically deformable contour models. *IEEE Transactions on Pattern Analysis and Machine Intelligence (PAMI)*, 14(11):1061–1075, Nov 1992.

J Stough, SM Pizer, EL Chaney, and M Rao. Clustering on image boundary regions for deformable model segmentation. In *International Symposium on Biomedical Imaging (ISBI)*, pages 436–439, Piscataway, NJ, April 2004. IEEE. ISBN 0780383893.

Martin Styner, Jeffrey A. Lieberman, and Guido Gerig. Boundary and medial shape analysis of the hippocampus in schizophrenia. *Medical Image Analysis (MedIA)*, April 2004. in press.

Martin A. Styner, Kumar T. Rajamani, Kutz-Peter Nolte, Gabriel Zsemlye, Gabor Szekely, Chris J. Taylor, and Rhodri H. Davies. Evaluation of 3D correspondence

methods for model building. In *Information Processing in Medical Imaging (IPMI)*, volume 2732 of *Lecture Notes in Computer Science*, pages 63–75. Springer, 2003. ISBN 3-540-40560-7.

H. Tek and B.B. Kimia. Volumetric segmentation of medical images by three-dimensional bubbles. *Computer Vision and Image Understanding (CVIU)*, 65(2):246–258, 1997.

Bart M. ter Haar Romeny, editor. *Geometry-Driven Diffusion in Computer Vision*. Computational Imaging and Vision. Kluwer Academic Publisher, 1994.

A. Tsai, W. Wells, C. Tempany, E. Grimson, and A. Willsky. Coupled multi-shape model and mutual information for medical image segmentation. In *Lecture Notes in Computer Science (LNCS): Information Processing in Medical Imaging (IPMI)*, volume 2732, pages 185–197. Springer-Verlag, 2003.

A. Tsai, W. Wells, C. Tempany, E. Grimson, and A. Willsky. Mutual information in coupled multi-shape model for medical image segmentation. *Medical Image Analysis (MedIA)*, September 2004. in press.

Gert Van de Wouwer. *Wavelets For Multiscale Texture Analysis*. PhD thesis, University of Antwerp, Belgium, 1998.

Bram van Ginneken, Alejandro F. Frangi, Joes J. Staal, Bart M. ter Haar Romeny, and Max A. Viergever. A non-linear gray-level appearance model improves active shape model segmentation. In A. Rangarajan L. Staib, editor, *IEEE Workshop on Mathematical Methods in Biomedical Image Analysis (MMBIA) 2001*, pages 205–212. IEEE Society Press, 2001.

Joachim Weickert, Seiji Ishikawa, and Atsushi Imiya. Linear scale-space has first been proposed in japan. *Journal of Mathematical Imaging and Vision*, 10:237–252, 1999.

L Willis. A geometric description of lung shape during respiration via mreps and normalized mutual information. Master's thesis, University of North Carolina at Chapel Hill, Department of Biomedical Engineering, 2001.

Alan S. Willsky. Multiresolution markov models for signal and image processing. *Proceedings of the IEEE*, 90(8):1396–1458, August 2002.

S. Zhu and A. Yuille. Region competition: Unifying snakes, region growing, and Bayes/MDL for multi-band image segmentation. In *International Conference on Computer Vision (ICCV)*, pages 416–423, 1995.